Received: Added at production | Revised: Added at production | Accepted: Added at production

DOI: xxx/xxxx

ARTICLE TYPE

A Bayesian Approach to Blood Rheological Uncertainties in Aortic Hemodynamics

Sascha Ranftl[1,3] | Thomas Stephan Müller[2,3] | Ursula Windberger[4] | Günter Brenn[2,3] | Wolfgang von der Linden[1,3]

[1]Institute of Theoretical and Computational Physics, Graz University of Technology, Petersgasse 16, 8010 Graz, Austria
[2]Institute of Fluid Mechanics and Heat Transfer, Graz University of Technology, Inffeldgasse 25/F, 8010 Graz, Austria
[3] Graz Center of Computational Engineering, Graz University of Technology, Krenngasse 37/II, 8010 Graz, Austria
[4]Center for Biomedical Research, Medical University of Vienna, Borschkegasse 8a, 1090 Vienna, Austria

Correspondence
*Sascha Ranftl. Email: ranftl@tugraz.at

Present Address
GCCE. Krenngasse 37/II. 8010 Graz

Abstract

Computational hemodynamics has received increasing attention recently. Patient-specific simulations require questionable model assumptions, e.g. for geometry, boundary conditions, and material parameters. Consequently, the credibility of these simulations is much doubted, and rightly so. Yet, the matter may be addressed by a rigorous uncertainty quantification. In this contribution, we investigated the impact of blood rheological models on wall shear stress uncertainties in aortic hemodynamics obtained in numerical simulations. Based on shear-rheometric experiments, we compare the non-Newtonian Carreau model to a simple Newtonian model and a Reynolds number-equivalent Newtonian model. Bayesian Probability Theory treats uncertainties consistently and allows to include elusive assumptions such as the comparability of flow regimes. We overcome the prohibitively high computational cost for the simulation with a surrogate model, and account for the uncertainties of the surrogate model itself, too. We have two main findings: 1) The Newtonian models mostly underestimate the uncertainties as compared to the non-Newtonian model. 2) The wall shear stresses of specific persons cannot be distinguished from one another due to largely overlapping uncertainty bands, implying that a more precise determination of person-specific blood rheological properties is necessary for person-specific simulations. While we refrain from a general recommendation for one rheological model, we have quantified the error of the uncertainty quantification associated with these modelling choices.

KEYWORDS:
Uncertainty Quantification; Aortic Hemodynamics; Blood Rheology; non-Newtonian fluids; Computational Fluid Dynamics; Bayesian Probability Theory

1 | INTRODUCTION

Recent efforts in computational biomechanics were directed towards better understanding pathologies, with the prospect of patient-specific simulations and improving clinical procedures. Cardiovascular diseases received particular interest since they cause half of all deaths worldwide[1], a large portion of which is attributed to pathological conditions of the aorta[2], e.g. aortic dissection. In aortic dissection, blood pushes through a tear in the inner aortic wall and delaminates the layers, forming a new cavity. The hemodynamics exert a mechanical stress on the aortic wall, and a popular hypothesis is that these wall shear stresses (WSS) are linked to aortic dissection[3]. Particularly, a reduced oscillatory shear index of these WSS has been associated with an increased risk of endothelial cell disease, e.g. tissue inflammation[4]. For blood flow modelling, blood is still widely assumed to be a Newtonian fluid also in large arteries, e.g. for simulations of aortic dissections[5], despite the fact that blood undoubtedly is a shear-thinning fluid. The importance of this shear-thinning behaviour in large arteries is still disputed.[6,7,8,9,10] deemed the influence of the shear-thinning behavior on the hemodynamics negligible, justified by the prevailing shear rates being in a regime of nearly constant viscosity. In contrast, other studies stress the importance of shear-thinning in complex geometries, such as the aorta[11,12,13,14].

All of these studies assumed a given set of parameters for their rheological models, but in a clinical scenario, these parameters are not given precisely. There may be a vague notion of the bounds on these parameters, or even a population statistic, yet the rheological parameters remain uncertain. These rheological uncertainties then enter the simulation, and subsequently any simulation result will be uncertain too. In this article, we shall quantify these rheological uncertainties.

The importance of uncertainty quantification (UQ) is already accepted in numerical flow mechanics[15] and biomechanics[16]. A comprehensive collection of reviews on UQ can be found in[17]. In[18], a statistician's perspective is discussed. Here, we will use Bayesian Probability Theory[19,20]. The uncertainties in hemodynamics simulations specifically are not completely understood yet. The main sources of uncertainty may be ascribed to (i) boundary conditions, (ii) geometry and (iii) material parameters. Scarce literature is available on quantification and/or propagation of (i) boundary condition uncertainties[21,22] and (ii) geometry uncertainties[23,24]. Regarding (iii) material parameters,[25] compared the uncertainties of different non-Newtonian viscosity models for small Reynolds numbers in an idealized bifurcation model of a vein, however surrogate uncertainties are neglected and ad-hoc assumptions on the parameter statistics made.[26] considered all sources (i-iii), however with a Newtonian viscosity only.

In this contribution, we discuss a Bayesian perspective on the viscosity uncertainties and how the uncertainties propagate to the aortic WSS. In contrast to previous work, we derive a coherent Bayesian theory and do not need ad-hoc assumptions. The uncertainty propagation demands a large number of simulations, i.e. a prohibitively large computational effort. A common workaround is to run the simulation for a few selected parameter values, and use that data to "learn" a surrogate model. The simulation

[0]**Abbreviations:** UQ, uncertainty quantification; BTP, Bayesian Probability Theory; FVM, Finite Volume Method; WSS, wall shear stress

uncertainties are then inferred from this surrogate model instead of the original simulation model at a significantly reduced computational effort. Popular surrogate models are Polynomial Chaos Expansion [27,28] and Gaussian Process Regression [29,30], the latter of which has had its renaissance recently from within the machine learning community. The reduction in computational effort however involves a trade-off for accuracy. The weak point of this procedure is the credibility of the surrogate model. Our Bayesian approach allows to include the uncertainties of this surrogate model itself, too.

We ultimately compare the uncertainties of the non-Newtonian model with the uncertainties of the Newtonian models, and how they affect the uncertainties of the hemodynamic shear stresses exerted on the aortic wall. We additionally compare personalized rheological models to population-averaged models.

The paper is organized as follows: Sec. 2 describes the methods and model assumptions regarding blood rheology and fluid dynamics. Sec. 3 describes the assumptions and statistical theory for the uncertainty quantification. Sec. 4 presents the results. In Sec. 5, the paper concludes.

2 | METHOD AND MODELLING: BLOOD RHEOLOGY AND AORTIC HEMODYNAMICS

The following section describes governing equations, rheological model, flow domain, boundary conditions and numerics. In the present work, we investigate aortic blood flow and the wall shear stress (WSS) on the aortic wall. The emphasis lies on uncertainties of WSS due to the uncertainty of the rheological model parameters.

2.1 | Fluid Dynamics - Governing Equations

The fluid is assumed incompressible, thus its density ρ is constant. Then the mass balance of a given control volume reduces to the requirement that the velocity field $\boldsymbol{u}$ must be solenoidal:

$$\boldsymbol{\nabla} \cdot \boldsymbol{u} = 0 \tag{1}$$

To formulate the equation of motion for a fluid, the momentum of the same control volume is balanced. Neglecting body forces yields

$$\rho \left[\frac{\partial \boldsymbol{u}}{\partial t} + (\boldsymbol{u} \cdot \boldsymbol{\nabla})\boldsymbol{u} \right] = \boldsymbol{\nabla} \cdot \boldsymbol{T} \tag{2}$$

The term on the right hand side is the divergence of the Cauchy stress tensor $\boldsymbol{T}$, which is split into two parts as per

$$\boldsymbol{T} = -p\boldsymbol{I} + \boldsymbol{\tau} \tag{3}$$

where p is the pressure, $\boldsymbol{I}$ the unit tensor, and $\boldsymbol{\tau}$ the extra stress tensor. The extra stress in the fluid depends on the instantaneous local flow field and on the rheological material behaviour. A constitutive model for the rheological properties needs to be defined in order to determine $\boldsymbol{\tau}$. Thermal energy is not balanced and the flow is assumed isothermal.

2.2 | Rheology

We introduce three different rheological models below: 1) the non-Newtonian Carreau model, 2) a Newtonian model that is Reynolds-number equivalent to the non-Newtonian Carreau model, and 3) a simple Newtonian model. We further document the shear-rheometric experiment. The three models' impact on the WSS uncertainty will later be compared.

2.2.1 | Non-Newtonian fluid

The choice of the rheological model is crucial because its behaviour determines the extra stress in the flow due to the velocity field. Experiments have shown that blood has a shear rate-dependent viscosity, which decreases as the shear rate increases[7]. An inelastic and shear rate dependent, i.e. shear-thinning, viscosity model is needed in our application. Thus, the formulation as in[31] for a generalized Newtonian model is chosen. The material model for the extra stress tensor $\boldsymbol{\tau}$ describing the inelastic shear-thinning behaviour is

$$\boldsymbol{\tau} = 2\eta(\dot{\gamma})\boldsymbol{D} \tag{4}$$

determined by the local rate-of-deformation tensor

$$\boldsymbol{D} = \frac{1}{2}\left(\nabla\boldsymbol{u} + (\nabla\boldsymbol{u})^{\mathsf{T}}\right) \tag{5}$$

given by the symmetrical part of the velocity gradient tensor $\nabla\boldsymbol{u}$ and the dynamic viscosity η as a function of the local shear rate $\dot{\gamma}$. In rheology, efforts have been made to find adequate mathematical model equations to represent such a rheological behaviour. Roughly divided, three model approaches have been established for the phenomenological description of the viscosity as a function of the shear rate in hemodynamics. Namely, models of the type power-law[32], Casson[33] and Carreau[34]. It is important that the model is valid for all occuring shear rates between high and low. As such, the Carreau model formulation is chosen, which reads

$$\eta(\dot{\gamma}) = \eta_\infty + (\eta_0 - \eta_\infty)\Big[1 + (\lambda\dot{\gamma})^2\Big]^{(n-1)/2}. \tag{6}$$

η_0 represents the asymptotic zero-shear viscosity (1st Newtonian plateau) and η_∞ equals the limiting value for high shear rates (2nd Newtonian plateau). λ and n determine shape and slope of the non-linear regime. Parameters and uncertainties are estimated

from shear-rheometric experiments described below. The shear rate $\dot{\gamma}$ is given as in[35].

$$\dot{\gamma} = \left(2\mathrm{tr}(\boldsymbol{D}^2)\right)^{1/2} \tag{7}$$

2.2.2 | Reynolds number-equivalent Newtonian fluid

We aim at a fair comparison of the rheological models through comparable flow regimes achieved by a dimensional analysis. In case of a Newtonian fluid, the viscosity is independent of the shear rate and constant. This simplifies eq. 4. In order to characterize a flow, a dimensional analysis enables the identification of a set of non-dimensional parameters. Therefore, all quantities characterising the flow, including the fluid properties, need to be identified. $\overline{(.)}$ denotes the spatial, and $\tilde{(.)}$ the temporal average of a quantity (.). The given problem is governed by the following quantities: $\tilde{\overline{u}}$ the cardiac output equivalent velocity, the difference $\Delta\overline{u}$ between the peak systolic velocity and minimal diastolic velocity, the angular frequency ω of the pulsation (heart rate), the diameter $\mathrm{D_{AA}}$ of the vessel, and the density ρ and dynamic viscosity η of blood. From these six quantities, three non-dimensional numbers can be derived[36]

$$\mathrm{Re} = \frac{\tilde{\overline{u}}\mathrm{D_{AA}}\rho}{\eta}; \quad \mathrm{Wo} = \frac{\mathrm{D_{AA}}}{2}\sqrt{\frac{\overline{\omega\rho}}{\eta}}; \quad \mathrm{I_p} = \frac{\Delta\overline{u}}{\tilde{\overline{u}}} \tag{8}$$

The Reynolds number Re represents the ratio of convective to diffusive transport of momentum. Due to the variable viscosity, the Reynolds number requires a special treatment. We adapted the generalized Reynolds number in non-Newtonian flows proposed by[37] for a power-law fluid to the rheological model in eq. 6.

The result is

$$\begin{aligned}
\mathrm{Re_{gen}} &= \frac{\tilde{\overline{u}}^2\rho}{\frac{3m+1}{4m}\left(\frac{\tilde{\overline{u}}}{\mathrm{D_{AA}}}\right)\left[\eta_\infty + (\eta_0-\eta_\infty)\left[1+\left(\lambda\frac{3m+1}{4m}\left(8\frac{\tilde{\overline{u}}}{\mathrm{D_{AA}}}\right)\right)^2\right]^{\frac{n-1}{2}}\right]} \\
m &= \frac{\eta_\infty + (\eta_0-\eta_\infty)\left[\left[1+(\lambda\dot{\gamma}_w)^2\right]^{(n-1)/2} + (\lambda\dot{\gamma}_w)^2(n-1)\left(1+(\lambda\dot{\gamma}_w)^2\right)^{(n-3)/2}\right]}{\eta_\infty + (\eta_0-\eta_\infty)\left[1+(\lambda\dot{\gamma}_w)^2\right]^{(n-1)/2}}
\end{aligned} \tag{9}$$

with the wall shear rate $\dot{\gamma}_w = \frac{3m+1}{4m}\left(8\frac{\tilde{\overline{u}}}{\mathrm{D_{AA}}}\right)$. The latter equation for m is solved iteratively starting from an initial value (here, $m_0 = 0.5$). The iteration is stopped when the difference of two successive values for m is less than 10^{-5}. This results in a Reynolds number-equivalent constant dynamic viscosity. In more detail, the generalized Reynolds number is calculated for the non-Newtonian viscosity model. The generalized Reynolds number is then used to determine a Newtonian viscosity with equivalent Reynolds number to ensure comparable flow regimes at the aortic root. Given a non-Newtonian viscosity, this procedure delivers the apparent (time-averaged and space-averaged) Newtonian viscosity that preserves the flow resistance and yields the same pressure difference between inlet and outlet. With μ being the Newtonian viscosity equivalent to the non-Newtonian

viscosity, as defined from the generalized Reynolds number, this formally is

$$\mu = \frac{\tilde{\bar{u}} \mathrm{D_{AA}} \rho}{\mathrm{Re_{gen}}} \tag{10}$$

The second dimensionless number is the Womersley number Wo[38]. It is a ratio of oscillatory to viscous time scales. Analogously to the Reynolds number, the non-Newtonian viscosity demands a generalized form. The following expression for the Womersley number results:

$$\mathrm{Wo} = \frac{1}{2}\sqrt{\frac{\mathrm{D_{AA}}\omega}{\tilde{\bar{u}}}\mathrm{Re_{gen}}} \tag{11}$$

The third dimensionless number is given by Gosling's pulsatility index (PI)[39] in eq. 8.

2.2.3 | Simple Newtonian fluid

We use an established model for the Newtonian blood viscosity by Merrill[7]:

$$\eta_{bl} = \eta_{pl}\left[1 + 2.5 \cdot 10^{-2} H + 7.35 \cdot 10^{-4} H^2\right] . \tag{12}$$

η_{bl} and η_{pl} are the dynamic viscosity of blood and plasma, respectively, and hematocrit H is in units of [%]. $\eta_{pl} = (1.2 \pm 0.1)\, mPas$ was reported in[40]. We chose a hematocrit of $H = 40\%$ for all simulations. Note that this simple Newtonian model is not Reynolds number-equivalent, in contrast to the Newtonian model defined previously in Sec. 2.2.2. We will later compare the non-Newtonian model and the Reynolds number-equivalent Newtonian model in the context of this simple Newtonian model as the standard.

2.2.4 | Rheological Experiments

Rheological properties of human blood were measured in simple shear at a temperature of 37° in a shear rheometer with a double cylindrical gap geometry for shear rates ranging from $1\,\mathrm{s}^{-1}$ to $1000\,\mathrm{s}^{-1}$ (Anton Paar DG26.7/Q1/TI-SN35200. inner gap: 0.417 *mm*, outer gap: 0.462 *mm*, radii: 13.769 *mm* and 12.33 *mm*). The experimental data originate from five volunteers, each sample was adjusted to the corresponding hematocrit values of 30 %, 40 %, 50 % and 60 % by centrifugation.

2.3 | Flow domain

We focus on the rheological aspects and use a simplified aortic geometry, i.e. a bent pipe with a circular cross section, to avoid uncertainties associated with the geometry, e.g. MRT/CT, rendering, interpolation or meshing. Fig. 1 shows the geometry. The circular cross section of the pipe has a constant diameter $\mathrm{D_{AA}}$ over the entire flow domain. $\mathrm{L_{AA}}$ is the ascending length of the aorta and the aortic arc has the radius $\mathrm{R_{Arc}}$ with a curvature angle of 180° ending in the descending

part of the aorta, which is of the length L_{DA}. The various lengths are listed in table 1. The carotid arteries and other branches were not taken into account in the modelling. At the points A to J, the simulation results will later be evaluated.

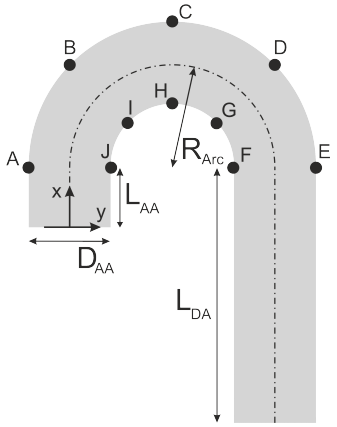

Figure 1 2D view of the 3D geometry.

Parameter	Value [mm]
D_{AA}	24
L_{AA}	18
R_{Arc}	30
L_{DA}	75

Table 1 Parameters of the geometry.

2.4 | Boundary Conditions

The velocity profile at the inlet is assumed to be of parabolic shape. Its distribution over the cross section for the given volumetric flow rate $Q(t)$ is given by

$$u_x(y,z,t) = \frac{2Q(t)}{\pi R^2}\left(1 - \frac{y^2+z^2}{R^2}\right) \quad \text{at} \quad x = 0 \tag{13}$$

$R{=}D_{AA}/2$ is the radius of the inlet cross-section. The temporal profile of the volumetric flow rate $Q(t)$ (fig. 2) was adapted from[41]. The boundary condition for the walls is the no-slip condition for the velocity, and the pressure is set to zero at the outlet. .

2.5 | Investigated Cases

The uncertainty analysis was carried out for three different cases corresponding to three different physiological states. The physiological state is characterized by the cardiac output $\tilde{Q}$ (CO), i.e. the mean volumetric flow rate over one cardiac cycle, which is defined as the volume of blood pumped by the heart per unit of time. So it is the product of the stroke volume V_{stroke} (SV), and the heart rate f_{heart} (HR, given by $\omega/2\pi$):

$$\tilde{Q} = V_{stroke} \cdot f_{heart} \tag{14}$$

The first case corresponds to a person at rest with a relatively low stroke volume and low heart rate at the same time (**LoRe_LoWo**). The second case (**HiRe_LoWo**) represents a person at rest, i.e. low heart rate, but with twice the stroke volume of the first case. The third case (**HiRe_HiWo**) corresponds to a person at moderate activity, i.e. higher demand of cardiac output and increased stroke volume and heart rate. The average volumetric flow rate equals that of the second case. The ranges of the absolute parameters and non-dimensional numbers were set according to data available from literature[42,43,44], and the

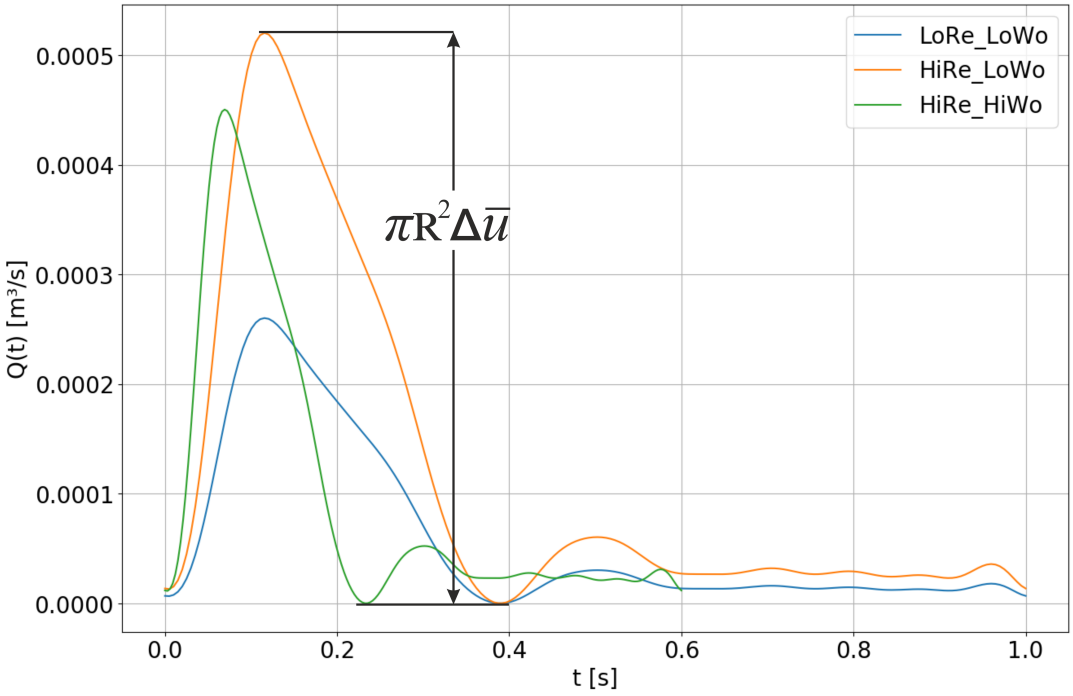

Figure 2 Transient profile of volumetric flow rate over one cardiac cycle, constructed with 13 harmonics.

Table 2 Parameters for the three physiological states. The hematocrit was 40 %.

Physiological State		**1: LoRe/LoWo**	**2: HiRe/LoWo**	**3: HiRe/HiWo**
Cardiac output $\tilde{Q}$	[L/min]	3.514	7.027	7.027
Stroke Volume V_{stroke}	[mL]	58	117	70
Frequency f_{heart}	[Hz]	1.0	1.0	1.67
Pulsatility index I_p	[-]	4.17	4.17	4.44

hematocrit was 40%. The parameters for the three cases are documented in table 2. The uncertainties of the rheological models described above are compared for these three physiological states. The comparison of the uncertainties of these three cases allows an insight into how the uncertainties are affected by the non-linear modelling itself.

2.6 | Numerics

Eq. 1 and eq. 2 were solved numerically using the finite volume method of the open source software *OpenFOAM*. The discretization of the geometry was achieved using Ansys ICEM 2019 R1 with a structured O-grid solely consisting of hexahedral cells for minimal geometric distortion and non-orthogonality. The mesh was gradually refined towards the wall to correctly resolve the gradients near the wall surface. A grid independence study of the velocity profiles was carried out with a steady volumetric flow rate at the inlet. A mesh independent solution of the velocity profiles was obtained with ∼ 290000 cells. Accordingly, this grid was used for the simulations. A first-order implicit scheme was chosen for time derivatives for which the time step was

adaptively adjusted to the velocity field in order to keep the Courant number below a value of 0.9, ensuring numerical stability and decreasing the simulation time. Gradient and divergence schemes were calculated with second-order central differences. In addition, gradients were limited with a multi-dimensional limiter to reduce numerical diffusion. The non-orthogonality of wall-normal gradients was taken into account with surface normal gradient scheme. A solution periodic in time was obtained for all the transient simulations.

3 | METHOD AND MODELLING: BAYESIAN UNCERTAINTY QUANTIFICATION

The goal is to quantify the uncertainties of the simulation results for the shear stress at different points on the inner aortic wall. The WSS are obtained from numerical simulations (finite volume method), based on the (non-) linear viscosity models discussed in the previous section. The latter depends on unknown parameters $\boldsymbol{a}$, which shall be inferred from the data $\boldsymbol{d}_{\text{exp}}$ obtained in rheological experiments. It is proven mathematically in[45] and references therein that Bayesian Probability Theory (BPT) is unique and the only consistent calculus for partial truths or rather uncertainty quantification. The Bayesian approach to uncertainty quantification developed here is accordingly inspired by[46,20]. For the readers unfamiliar with BPT, we provide a brief introduction in Appendix A. In Sec. 3.1, we apply BPT to analyze the experimental viscosity data (as described in Sec. 2.2) to infer the uncertainty of the Carreau parameters. In Sec. 3.2, these uncertainties are then propagated through the subsequent Computational Fluid Dynamics simulation of aortic hemodynamics to obtain the uncertainty of the WSS. Analogous discussions concern the Reynolds number-equivalent Newtonian model and the simple Newtonian model.

3.1 | Bayesian Analysis of Rheological Experiments

Here, we quantify the uncertainties of the viscosity parameters based on shear-rheometric experiments (Sec. 2.2.4). In the Carreau model in eq. 6 , the viscosity η is a function of the shear rate $\dot{\gamma}$ and parametrized by $\{\eta_\infty, \eta_0, \lambda, n\}$. For notational convenience, we re-label the parameters to $\boldsymbol{a} \equiv \{a_1, a_2, a_3, a_4\}$. with

$$a_1 := \eta_\infty \, , a_2 := \eta_0 - \eta_\infty \, , a_3 := \lambda \, , a_4 := -\frac{n-1}{2} \, . \tag{15}$$

The measured viscosity is corrupted by additive noise ε, i.e.

$$\eta = f(\dot{\gamma}|\boldsymbol{a}) + \varepsilon \, , \tag{16}$$

$$f(\dot{\gamma}|\boldsymbol{a}) := a_1 + a_2(1 + a_3^2\dot{\gamma}^2)^{-a_4} \, . \tag{17}$$

Applying Bayes' theorem to the rheology data set $\boldsymbol{d}_{\text{exp}} = \{\boldsymbol{\eta}, \dot{\boldsymbol{\gamma}}\}$ yields

$$p\big(\boldsymbol{a} \mid \boldsymbol{d}_{\text{exp}}\big) = p\big(\boldsymbol{a} \mid \boldsymbol{\eta}, \dot{\boldsymbol{\gamma}}\big) = \frac{1}{Z}\, p\big(\boldsymbol{\eta} \mid \boldsymbol{a}, \dot{\boldsymbol{\gamma}}\big) p(\boldsymbol{a}) \tag{18}$$

The normalization Z is not required. The other two factors, likelihood and prior will be discussed next.

3.1.1 | The Likelihood function

We use experimental data of the blood viscosity η measured for a set of shear rates $\dot{\boldsymbol{\gamma}} = \{\dot{\gamma}_m\}_{m=1}^{N_m}$ on N_p volunteers. The experimental viscosities of volunteer $n \in \{1, \dots, N_p\}$ for shear rate $m \in \{1, \dots, N_m\}$ are denoted by η_{mn} and combined in the vector $\boldsymbol{\eta}_n$ for each volunteer and the matrix $\boldsymbol{\eta} = (\boldsymbol{\eta}_1, ..., \boldsymbol{\eta}_{N_m})$ for all volunteers. We note that in the actual experiment not all volunteers' samples have been measured at all N_m shear rates $\dot{\gamma}_m$. To avoid notation overload, this is not accounted for in the following notation, but taken into account correctly in the evaluation. We assume a Gaussian measurement error ε, and so the likelihood of a single data point η_{mn} is

$$p\big(\eta_{mn} \mid \dot{\gamma}_m, \boldsymbol{a}, \sigma_m\big) = \frac{1}{\sqrt{2\pi\sigma_m^2}} \exp\left(- \frac{(\eta_{mn} - f(\dot{\gamma}_m|\boldsymbol{a}))^2}{2\sigma_m^2} \right). \tag{19}$$

The experimental error may depend on the shear rate $\dot{\gamma}_m$ but not on the person. The data suggest that the standard deviation, σ_m, is inversely proportional to the logarithm of the shear rate $\dot{\gamma}_m$,

$$\sigma_m = \alpha \hat{\sigma}_m\,, \tag{20a}$$

$$\hat{\sigma}_m^2 = \frac{1}{\log(\dot{\gamma}_m) + 1}\,, \tag{20b}$$

with scaling factor α. This is motivated by estimates of the variance at given shear rates. The measured shear rates range from $10^0\ s^{-1}$ to $10^3\ s^{-1}$, hence $+1$ is added to ensure $\hat{\sigma}_m$ is real at low shear rates. Assuming that the measurement errors at different shear rates are uncorrelated, the likelihood for a specific person is

$$p\big(\boldsymbol{\eta}_n \mid \dot{\boldsymbol{\gamma}}, \boldsymbol{a}, \alpha\big) = \prod_{m=1}^{N_m} p\big(\eta_{mn} \mid \dot{\gamma}_m, \boldsymbol{a}, \alpha\big) = \frac{1}{Z} \alpha^{-N_m} \exp\left(- \frac{\chi_n^2}{2\alpha^2} \right) \tag{21}$$

$$\chi_n^2 = \sum_m \frac{\big(\eta_{mn} - f(\dot{\gamma}_m|\boldsymbol{a})\big)^2}{\hat{\sigma}_m^2}\,. \tag{22}$$

Since the measurements for different persons are uncorrelated, the likelihood for the population is

$$p\big(\boldsymbol{\eta} \mid \dot{\boldsymbol{\gamma}}, \boldsymbol{a}, \alpha\big) = \prod_{n=1}^{N_p} p\big(\boldsymbol{\eta}_n \mid \dot{\boldsymbol{\gamma}}, \boldsymbol{a}, \alpha\big) = \frac{1}{Z} \alpha^{-N} \exp\left(- \frac{\chi^2}{2\alpha^2} \right) \tag{23}$$

$$\chi^2 = \sum_n \chi_n^2 \tag{24}$$

with $N = N_m N_p$. From the normalization constant of the likelihood we have only mentioned explicitly the α dependence, as it will become important in the next step. α is an unknown hyper parameter, which has to be marginalized over with the appropriate Jeffreys' prior for scale variables, i.e. $p(\alpha) \propto 1/\alpha$. Then the resulting marginal likelihood is a Student-t distribution

$$p\big(\boldsymbol{\eta}_n \mid \dot{\boldsymbol{\gamma}}, \boldsymbol{a}\big) = \frac{1}{Z'}(\chi_n^2)^{-\frac{N_m}{2}} \tag{25}$$

$$p\big(\boldsymbol{\eta} \mid \dot{\boldsymbol{\gamma}}, \boldsymbol{a}\big) = \frac{1}{Z''}(\chi^2)^{-\frac{N}{2}} \ , \tag{26}$$

where the normalization constants Z' and Z'' are irrelevant for our purposes. This model is robust to outliers, a property very favourable in the light of the large physiological variability.

3.1.2 | The prior

BPT allows to rigorously and consistently incorporate any prior knowledge about the experiment before taking a look at the data. This knowledge shall be elicited here. The viscosity is modeled by a generalized power-law (Eq. 6). It is reasonable to assume that our inference must not depend on the exact parametrization. I.e. if we re-label the parameters, the results must not change. This rescaling-invariance is ensured by Jeffreys' generalized prior and is given by the Riemann metric $\boldsymbol{R}$ (or the determinant of the Fisher information matrix)[19]

$$p(\boldsymbol{a}) = \frac{1}{Z}\Big|\det(\boldsymbol{R})\Big|^{1/2} \tag{27}$$

$$R_{ij} = \int p\big(\boldsymbol{\eta} \mid \dot{\boldsymbol{\gamma}}, \boldsymbol{a}\big) \frac{\partial^2}{\partial a_i \partial a_j} \ln\Big(p\big(\boldsymbol{\eta} \mid \dot{\boldsymbol{\gamma}}, \boldsymbol{a}\big)\Big)\, dV_{\boldsymbol{\eta}} \ . \tag{28}$$

With the likelihood defined above, the result is (see Appendix B)

$$R_{ij} \propto \sum_{m=1}^{N} \frac{1}{\hat{\sigma}_m^2} \frac{\partial f(\dot{\gamma}_m \mid \boldsymbol{a})}{\partial a_i} \frac{\partial f(\dot{\gamma}_m \mid \boldsymbol{a})}{\partial a_j} \ . \tag{29}$$

where either $N = N_m$ (person-specific likelihood) or $N = N_m N_p$ (population likelihood). The derivatives are available analytically by routine mathematics. This prior is the least-informative prior that adheres to the physical requirement that the viscosity does not depend on the units of the parameters $(\eta_0, \eta_\infty, \lambda, n)$, i.e. the units (scales) of the parameters can be set arbitrarily as long as they are consistent. A particular strength of this prior, in contrast to a flat prior, here is that it ensures a normalizeable posterior and results are not sensitive to the choice of any hyperparameters, e.g. integration bounds. In addition to the reparametrization-invariance, we also have the prior knowledge that viscosities are positive. That is ensured by $a_1 \geq 0$, $a_2 \geq 0$, $a_1 + a_2 \geq 0$. Moreover, the viscosity decreases with increasing shear rate, i.e. $a_4 > 0$. Finally, we can restrict the third parameter to $a_3 \geq 0$ as it only enters quadratically. We note that incorporating the scale-invariance greatly increases the authority of the results. Prior information is important in the case of weak data information. This is the case here as far as the individual parameters a_2 and a_3 are concerned.

3.1.3 | Parameter and Viscosity Estimation and associated Uncertainties

With Bayes' theorem given in eq. 18 we can now compute the joint posterior probability density function (pdf) for all Carreau parameters, $p(\boldsymbol{a} \mid \boldsymbol{d}_{\text{exp}})$. The marginal posterior pdf for one specific parameter is given by the integral with respect to the remaining parameters, e.g.

$$p(a_1 \mid \boldsymbol{d}_{\text{exp}}) = \int dV_{a_2} \int dV_{a_3} \int dV_{a_4}\, p(\boldsymbol{a} \mid \boldsymbol{d}_{\text{exp}}) \,. \tag{30}$$

The probabilities for the other parameters are computed analogously. Similarly, joint pdf-s for any combination of parameters, such as $p(a_1, a_2 \mid \boldsymbol{d}_{\text{exp}})$, are obtained by the volume integral with respect to the remaining parameters a_3 and a_4.

Another interesting topic is regression, i.e. we want to determine the pdf for the viscosity $\eta_{\dot\gamma}$ for a specific shear rate $\dot\gamma$, based on the measured rheological data, i.e. $p(\eta \mid \dot\gamma, \boldsymbol{d}_{\text{exp}})$. The background information includes the fact that we use the Carreau model for the viscosity. The estimated viscosity $\eta_{\dot\gamma}$ for a shear rate $\dot\gamma$ of interest is then given by the marginalization rule (eq. A1)

$$p(\eta_{\dot\gamma} \mid \dot\gamma, \boldsymbol{d}_{\text{exp}}) = \int dV_{\boldsymbol{a}} p(\eta_{\dot\gamma} \mid \boldsymbol{a}, \dot\gamma, \cancel{\boldsymbol{d}_{\text{exp}}}) p(\boldsymbol{a} \mid \dot\gamma, \boldsymbol{d}_{\text{exp}}) \,. \tag{31}$$

Obviously, insignificant conditionals have been striked out. The second pdf has already been determined. The first pdf is simply a Dirac delta because the background information tells us to use the Carreau model $\boldsymbol{f}(\dot\gamma \mid \boldsymbol{a})$ (eq. 17) to compute the viscosity and the required parameters are also given. Hence

$$p(\eta_{\dot\gamma} \mid \boldsymbol{a}, \dot\gamma) = \delta\left[\eta_{\dot\gamma} - f(\dot\gamma \mid \boldsymbol{a})\right] \,. \tag{32}$$

Consequently, mean and second moment of $\eta_{\dot\gamma}$ are simply

$$\langle \eta_{\dot\gamma} \rangle = \int f(\dot\gamma|\boldsymbol{a})\, p(\boldsymbol{a} \mid \boldsymbol{d}_{\text{exp}}) dV_{\boldsymbol{a}} \,, \tag{33}$$

$$\langle \eta_{\dot\gamma}^2 \rangle = \int \left(f(\dot\gamma|\boldsymbol{a})\right)^2 p(\boldsymbol{a} \mid \boldsymbol{d}_{\text{exp}})\, dV_{\boldsymbol{a}} \,. \tag{34}$$

From that we obtain the uncertainty

$$\Delta\langle \eta_{\dot\gamma} \rangle = \sqrt{\langle \eta_{\dot\gamma}^2 \rangle - \langle \eta_{\dot\gamma} \rangle^2} \,. \tag{35}$$

It should be emphasized that the Bayesian approach has two important advantageous over ad-hoc approaches. Firstly, common practise would be to determine the Maximum Likelihood estimate for the Carreau parameters $\boldsymbol{a}^{(\text{ML})}$ based on the data $\boldsymbol{d}_{exp}$, which in the Gaussian case is equivalent to minimizing the misfit. This parameter vector $\boldsymbol{a}^{(\text{ML})}$ is then used to determine the estimate for the viscosity by

$$\eta_{\dot\gamma}^{(\text{ML})} = f(\dot\gamma|\boldsymbol{a}^{(\text{ML})}). \tag{36}$$

This is not the same as the consistent use of the data and all available information, given by the Bayesian result. The latter yields only the same answer if the prior is negligible as compared to the likelihood, and if the likelihood is sharply peak at its maximum. The first condition is met if we have very many data points. The second condition is rarely fulfilled, particularly not in the present case, as we will see in the discussion of the results. Another very important advantage of the Bayesian approach is that it allows to determine the uncertainty on the same probabilistic footing.

3.1.4 | Probability for Reynolds numbers

The posterior $p(\boldsymbol{a} \mid \boldsymbol{d}_{\text{exp}})$ also allows to infer the pdf for the Reynolds number Re_{gen} and the equivalent Newtonian viscosity μ as

$$p(\text{Re}_{\text{gen}} \mid \boldsymbol{d}_{\text{exp}}) = \int \underbrace{p(\text{Re}_{\text{gen}} \mid \boldsymbol{d}_{\text{exp}}, \boldsymbol{a})}_{\delta[\text{Re}_{\text{gen}} - \text{Re}_{\text{gen}}(\boldsymbol{a})]} p(\boldsymbol{a} \mid \boldsymbol{d}_{\text{exp}})\, dV_{\boldsymbol{a}} \tag{37}$$

$$p(\mu \mid \boldsymbol{d}_{\text{exp}}) = \int \underbrace{p(\mu \mid \boldsymbol{d}_{\text{exp}}, \boldsymbol{a})}_{=\delta\left[\mu - \mu\left(\text{Re}_{\text{gen}}(\boldsymbol{a})\right)\right]} p(\boldsymbol{a} \mid \boldsymbol{d}_{\text{exp}}) dV_{\boldsymbol{a}} \tag{38}$$

where we have used the marginalization rule (eq. A1) and the background information that $\text{Re}_{\text{gen}}(\boldsymbol{a})$ and $\mu(\text{Re}_{\text{gen}})$ are defined by eq. 9 and eq. 10. The distribution of Womersley numbers can be computed analogously. The integrals can be evaluated numerically.

3.2 | Bayesian Uncertainty Propagation through the CFD simulation

The uncertainties of the blood rheological parameters have been calculated above, and are now propagated to the simulated wall shear stresses in the aorta. This is done for the three different rheological models defined in 2.2 (non-Newtonian Carreau model, Reynols-number equivalent Newtonian model, and simple Newtonian model).

3.2.1 | Non-Newtonian fluid

The uncertainty of the Carreau parameters $\boldsymbol{a}$ entails an uncertainty in the wall shear stress. Let $\boldsymbol{\tau} = (\tau_x, \tau_y, \tau_z)^T$ be the wall shear stress vector. Then let $w = ||\boldsymbol{\tau}||$ be the absolute value of the wall shear stress vector, or short absolute wall shear stress, at location x and time-instance t, denoted by $w^{(x,t)}$,

$$\langle w^{(x,t)} \rangle = \int w^{(x,t)} p(\boldsymbol{a} \mid \boldsymbol{d}_{\text{exp}}, \mathcal{I}) dV_{\boldsymbol{a}} \tag{39}$$

The uncertainty of this estimate is given by the diagonals of

$$\left\langle \Delta w^{(x,t)} \Delta w^{(x,t)} \right\rangle = \left\langle w^{(x,t)} w^{(x',t')} \right\rangle - \left\langle w^{(x,t)} \right\rangle \left\langle w^{(x',t')} \right\rangle \ . \tag{40}$$

with

$$\left\langle w^{(x,t)} w^{(x',t')} \right\rangle = \int w^{(x,t)} w^{(x',t')} p\left(\boldsymbol{a} \mid \boldsymbol{d}_{\text{exp}}, \mathcal{I}\right) dV_{\boldsymbol{a}} \tag{41}$$

The numerical evaluation of the integral over the four Carreau-parameters would imply the need for performing FVM-simulations at least 10^5 times, which is way too CPU expensive, as a single CFD simulations requires $\approx$ 18 h on 8 CPUs in parallel. This can be avoided if the FVM simulations are replaced by a surrogate model that approximates the WSS w by a suitably parametrized surrogate function $w_{\text{sur}} = g(\boldsymbol{a}|\boldsymbol{c})$, where $\boldsymbol{c}$ are yet unknown parameters. Clearly, the parameters of the surrogate model will also depend on those positions and the time instance. So we actually have

$$w_{\text{sur}}^{(x,t)} = g(\boldsymbol{a}|\boldsymbol{c}^{(x,t)}) = \sum_{\nu=1}^{N_b} c_\nu^{(x,t)} \phi_\nu(\boldsymbol{a}) \; . \tag{42}$$

where we have expanded the surrogate function in basis functions ϕ_ν. In our work, we chose multi-variate Legendre polynomials as basis w.l.o.g.. The unknown parameters $c_\nu^{(x,t)}$ will be inferred from a suitable training data set. To this end, FVM simulations are performed for a moderately sized set of Carreau parameters $\boldsymbol{A}_s = \{\boldsymbol{a}_s^{(i)}\}_{i=1}^{N_s}$ and the corresponding WSS, $\boldsymbol{W}_s$, are computed and combined in $\boldsymbol{D}_{\text{sim}} = \{\boldsymbol{A}_s, \boldsymbol{W}_s\}$. Now we use the background information, suggesting that we take the WSS w entering the integral in eq. 39 from the surrogate model rather than from the expensive FVM simulation. Under these assumptions, we can use the formulas derived in[47]. We emphasize that the underlying theory addresses the weak point of this approach by explicitly incorporating the surrogate uncertainties. The prior for the absolute value of the WSS was zero for negative values.

3.2.2 | Reynolds number-equivalent Newtonian fluid

Analogous to the procedure leading to eq. 38 and departing from the previous subsection, we find for the average and uncertainties of the WSS of the Reynolds number-equivalent Newtonian model

$$\langle w^{(x,t)} \rangle = \int w^{(x,t)} p\left(\mu \mid \boldsymbol{d}_{\text{exp}}, \mathcal{I}\right) dV_\mu \tag{43}$$

$$\langle w^{(x,t)} w^{(x',t')} \rangle = \int w^{(x,t)} w^{(x',t')} p\left(\mu \mid \boldsymbol{d}_{\text{exp}}, \mathcal{I}\right) dV_\mu \; . \tag{44}$$

$w^{(x,t)}$ is to be taken from the corresponding simulations with the Reynolds number-equivalent Newtonian fluid. The uncertainty of this estimate is then given analogously by eq. 40. No surrogate model is needed here since the one-dimensional integrals can be computed directly.

3.2.3 | Simple Newtonian fluid

The literature references in Sec. 2.2.3 assume that the pdf of the Newtonian viscosity is a Gaussian with mean and standard deviation documented therein. The same formulas as in Sec. 3.2.2 apply, where $p\left(\mu \mid \boldsymbol{d}_{\text{exp}}\right)$ is substituted with said Gaussian from the literature, and $w^{(x,t)}$ is to be taken from the corresponding simulations resulting with the simple Newtonian fluid.

4 | RESULTS

All numerical integrals for the uncertainty quantification were computed with Riemannian quadrature and convergence checked with successive grid refinement. Data and code is available in[48].

4.1 | Rheology

Here, we compare rheological results. We first compare the posterior probability density functions for the viscosity parameters, and its consequences for the viscosity (both non-Newtonian and Reynolds number-equivalent Newtonian) itself, for specific persons and the population-average. We then compare the population-averaged posterior probability density functions for the viscosity parameters, and its consequences for the non-Newtonian viscosity, for different hematocrits.

4.1.1 | Population-averaged vs. person-specific probabilities

Fig. 3a shows the posterior pdfs for the four Carreau parameters for two distinct volunteers and the population averages. Volunteer 1 shows two distinguished peaks in $a_1 := \eta_\infty$, and all pdfs are skewed and asymmetric. Apparently, the statistics cannot be sufficiently described with mean, maximum likelihood or variance alone. This argument is supported by the deformed banana shapes of the joint pdfs in fig. 3b-3d. The unusual shape of these pdfs poses no obstacle to our Bayesian uncertainty quantification. The inference is rather vague on the difference between the two plateaus of zero-shear limit viscosity to infinite-shear limit viscosity, $a_2 := \eta_0 - \eta_\infty$, and the slope, $a_3 := \lambda$, while the posterior for the infinite-shear limit viscosity alone , $a_1 := \eta_\infty$, covers a smaller range. In conjunction with the shear rate-dependent variance of the viscosity (eq. 20), this also causes larger uncertainty bands for the viscosity (fig. 4a) at low shear rates as compared to high shear rates. The tilt and 'narrow' width of the deformed 'ellipsis' of the panels 'a_2 vs. a_3' in fig. 3b-3d further mean, that the zero-shear plateau (offset) a_2 and the slope a_3 are strongly correlated. This in turn means, that better information on the zero-shear plateau, $a_2 \propto \eta_0$, would consequently allow to improve the inference on the slope, $a_3 := \lambda$, too, and vice versa. An analog statement can be made for the pair a_2 vs. a_4. The size of the ellipses however suggest that more or better data on either the slope or the zero-shear plateau (e.g. measurements at lower shear rates) are most promising for better estimates for the viscosity.

The population-averaged (fig. 3b) and person-specific (fig. 3c, 3d) pdfs live in the same region of parameter space and, albeit

translated slightly, overlap significantly. This behaviour translates further to the viscosities, fig. 4a. The estimated viscosities can be, naively, distinguished, however the uncertainty bands overlap considerably. The pdfs for the Reynolds number-equivalent Newtonian viscosity, fig. 4b, have a heavy tail, and are rather Student-t distributions than Gaussians. The person-specific results overlap considerably with population-averages. Notably, the distribution for volunteer 3 in physiological states 2-3 overlaps considerably with the population average in physiological state 1. This exemplifies the inadequacy of simple Newtonian models to account for state-dependent viscosity in the light of uncertainty, which is properly addressed in our approach via Reynolds number-equivalence.

4.1.2 | Population-averaged viscosities for different hematocrits

Fig. 5a shows the pdf for the Carreau parameters for different hematocrit values at otherwise same conditions, and fig. 5b the corresponding viscosity models. The viscosities are different at low shear rates including the non-linear regime, however uncertainty bands partially overlap at high shear rates. Each hematocrit's viscosity model can be easily distinguished as a whole though. Consequently, uncertainty bands derived from simulations based on these four viscosity models will not overlap, at least not due to the viscosity model. This implies that the hematocrit needs to be known within a small margin for person-specific simulations, albeit the quantification of this margin is not the matter of this work.

4.2 | Hemodynamics

We restrict our investigation to the case of hematocrit 40 %. For the non-Newtonian WSS, we used $N_s = 100$ training points in parameter space according to the design of the computer experiments (see appendix D), yielding a set of 100 simulations. Note that the computer experiments were designed to emphasize on the more important regions of high probability mass. An illustrative example of these primary results is shown in fig. 6. This data is then used to learn the surrogate models. It turned out that a total polynomial order of 2 is sufficient, corresponding to 15 basis functions in Eq. 42 (1 zeroth order, 4 first order, 10 second order, i.e. 10 distinct pairs $(a_i a_j)$. The amount of training data is thus roughly 3 times the amount typically recommended for Polynomial Chaos Expansions. Uncertainties are then computed with a Riemannian integration scheme on an equi-spaced $50 \times 50 \times 50 \times 50$ grid. No surrogate models were required for the Newtonian WSS, i.e. the uncertainties were determined directly from eq. 39 with a Riemannian integration scheme with 40 equally spaced pivot points. The design of the computer experiments yielded an acceptable surrogate uncertainty, comprising $< 1\%$ to $> 50\%$ in extreme cases of the total uncertainty , depending on location and time-instance. Note that the surrogate's uncertainty is assessed according to[47], and that the surrogate's uncertainty is directly included in and propagated to the uncertainty of the wall shear stress. This also means, that the corresponding standard paradigm of uncertainty quantification, e.g. with Polynomial Chaos Expansions or Kriging,

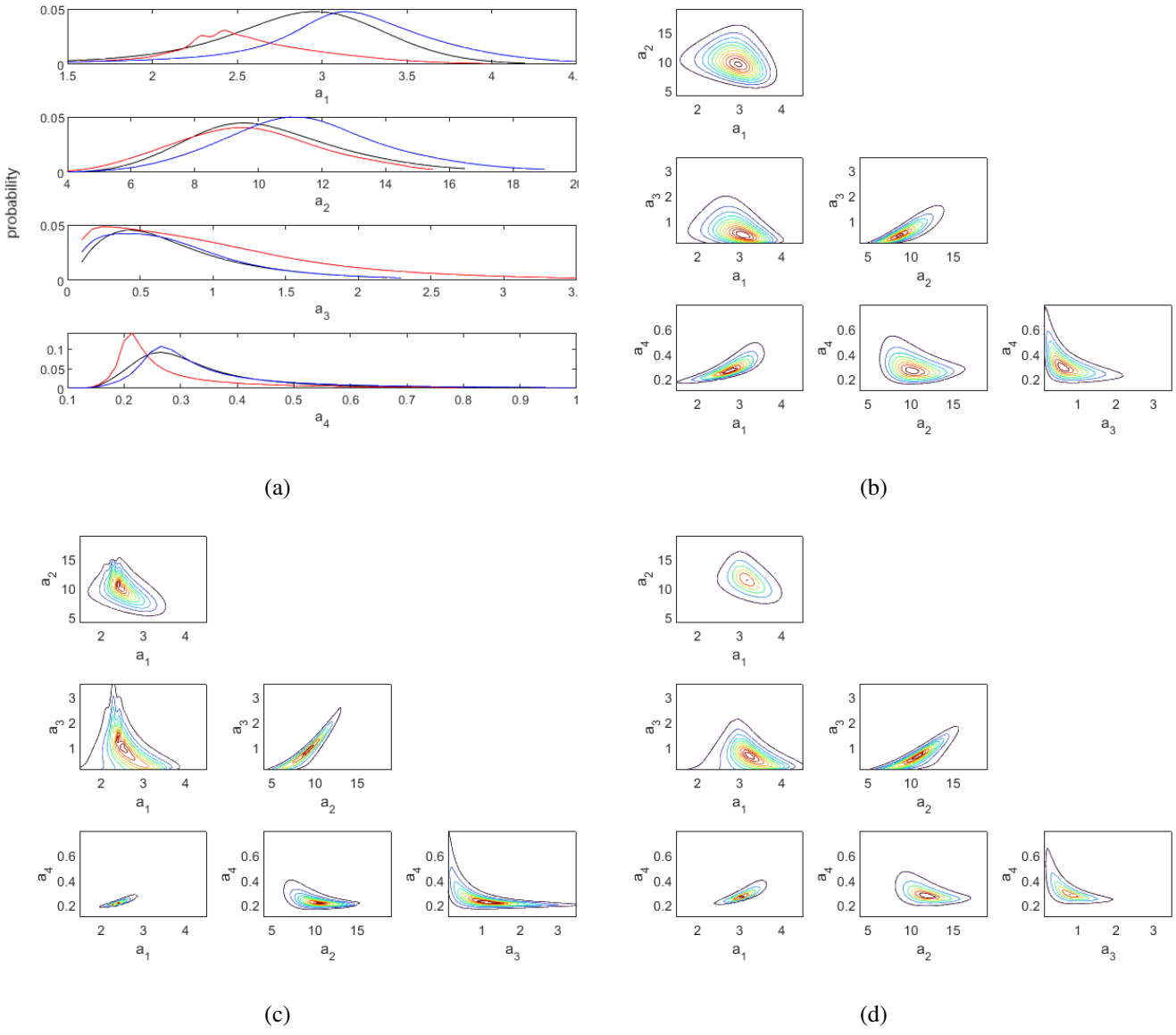

Figure 3 Results for the posterior probability distribution of the Carreau-model parameters (eq. 15, eq. 6) for a hematocrit of 40%. (a) Marginal posterior probabilities of the four parameters. Black is the population average, and red/blue is specific for volunteer 1/3. Panels (b-d) show contours of the joint marginal probability densities for the population-average (b), specific for volunteer 1 (c) and specific for volunteer 3 (d). The resulting posterior is far from being Gaussian or symmetric.

would neglect these surrogate uncertainties, and therefore naively underestimate the uncertainties precisely by the surrogate's contribution. Since all pdfs live in the same region of parameter space, the same surrogate can be used for all volunteers.

The results imply that a more precise determination of blood rheological properties is necessary for sensible person-specific simulations, e.g. by repeated or more precise measurements. If that is not possible, one might as well use population-averages. Further, the Newtonian models typically underestimate the uncertainty as compared to the non-Newtonian model. Although the authors are not aware of directly comparable studies with located probes, the resulting values generally agree with the ranges in the literature[49,50].

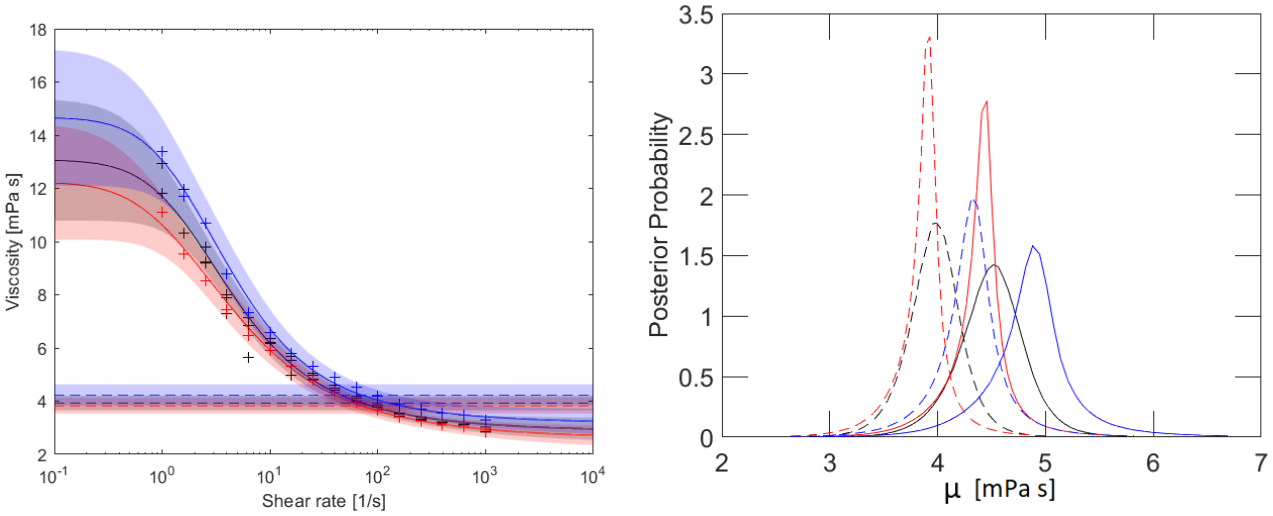

(a) (b)

Figure 4 (a) Viscosity over shear rate for a hematocrit of 40%. Black is the population average, and red/blue are person-specific (volunteer 1/3). + is the data, the continuous line is the estimate of the dynamic Carreau viscosity (Eq. 6) and the dashed line is the estimate of the corresponding Reynolds number-equivalent static viscosity (Eq. 38). Shaded areas are corresponding uncertainties with 1 standard deviation. (b) Posterior probability distribution for the Reynolds number-equivalent Newtonian viscosity μ according to Tab. 1 and Eq. 37. Colour code as in left panel. Solid (dashed) line: Physiological State 1 (2 & 3)

4.2.1 | Population-averaged vs. person-specific & moderate activity vs. at rest

In fig. 7b we compare the WSS of the non-Newtonian model for two volunteers and the population-average. Results and uncertainties overlap mostly. This raises two questions: 1) whether personalized viscosity measurements on this level of accuracy are necessary as opposed to population-averaged rheological parameters, and 2) whether personalized surrogate models (i.e. a surrogate as a function of rheological parameters) are really necessary, as opposed to population-average-based surrogate models. The results for population-averages may be deemed 'good enough' here, although this depends on the application. More importantly, the answer could be quite different if viscosity measurements were more precise or available in a larger range of shear rates. The overlap in fig. 7b was found to hold throughout and was expected, based on the similarity of fig. 3b- 3d. We proceed to compare different rheological models with population-averages only.

4.2.2 | Newtonian vs. non-Newtonian & moderate activity vs. at rest

We compare the population-averaged (fig. 3b) uncertainties of Newtonian and non-Newtonian models at different measurement locations (fig. 1) for the three different physiological states (table 2). We select four examples for demonstration, fig. 8. The wall shear stress (not its uncertainty) of the simple Newtonian model mostly lies between non-Newtonian model and Reynolds number-equivalent Newtonian model, however this model does not capture flow regime or shear-thinning. For a large part,

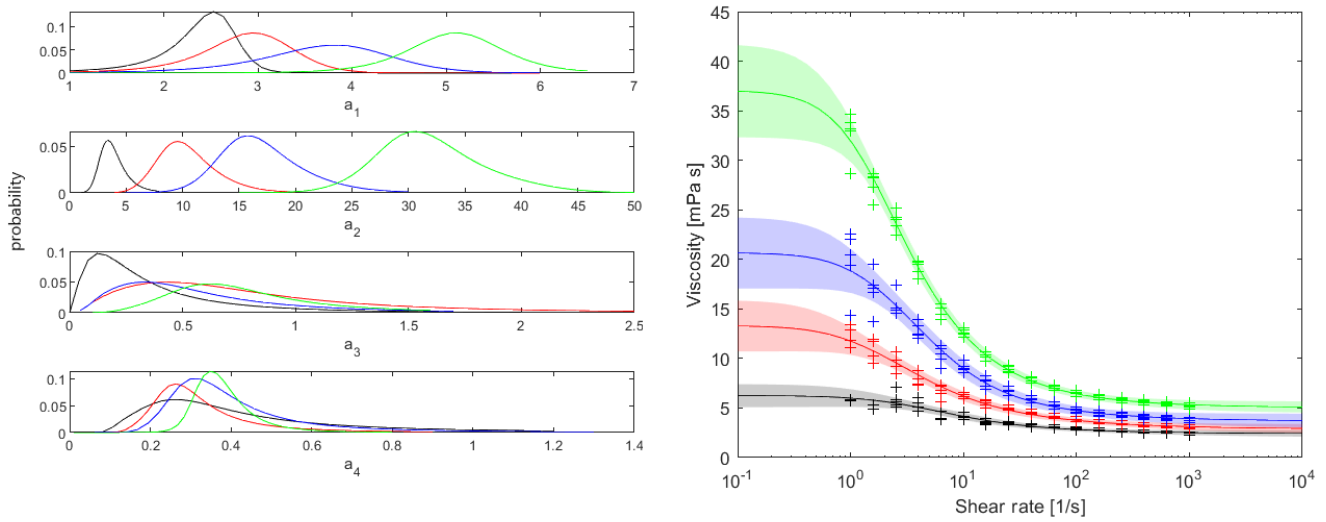

(a) (b)

Figure 5 (a) Population-averaged marginal probability densities (Eq. 30) for the four model parameters a_1, a_2, a_3, a_4 of the dynamic Carreau viscosity (Eq. 6). The colors black/red/blue/green belong to hematocritcs of 30%/40%/ 50%/60%. All pdfs are similar in shape, however shifted in a_1 and a_2. (b) shows viscosity over shear rate. The colors black/red/blue/green belong to hematocritcs of 30%/40%/ 50%/60%. + is the data, the continuous line is the estimate of the Carreau viscosity (Eq. 6) and the shaded areas are corresponding uncertainties.

both Newtonian models underestimate the uncertainty as compared to the non-Newtonian model uncertainty. However, the non-Newtonian uncertainties are not necessarily larger than the Newtonian model uncertainties. At specific time-instances, they can occasionally also be in between the two Newtonian models, see. e.g. fig. 8 b, bottom panel at ca 0.7 t/T. At specific locations, they can also be smaller than both Newtonian models, see e.g. row B of case 2 in Table E3 in Appendix E. Time-averaged wall shear stresses and oscillatory shear indices, that are sometimes used as 'biologically relevant indices', are not discussed in depth here, however are documented for the population-averaged posterior in Appendix E. The numbers demonstrate that both is possible, that a Newtonian model underestimates or overestimates the specific index or its uncertainty as compared to the non-Newtonian model. Whether the differences are 'biologically relevant', e.g. in terms of the response of the endothelial cells or arteriosclerosis, remains questionable.

4.3 | Further Discussion and Limitations

The adaption of this approach to other rheological models than the Carreau model (eq. 6) is in principle straight-forward. If the measurement error is assumed to be Gaussian, then the likelihood is also Gaussian. If the noise level of the Gaussian is not known, then the likelihood would be a Student-t. The resulting prior will have the form of eq. 29, and depend only on the rheological model's derivatives. Other measurement errors, e.g. of the form of a Gamma- or Beta-distribution or its variants, are

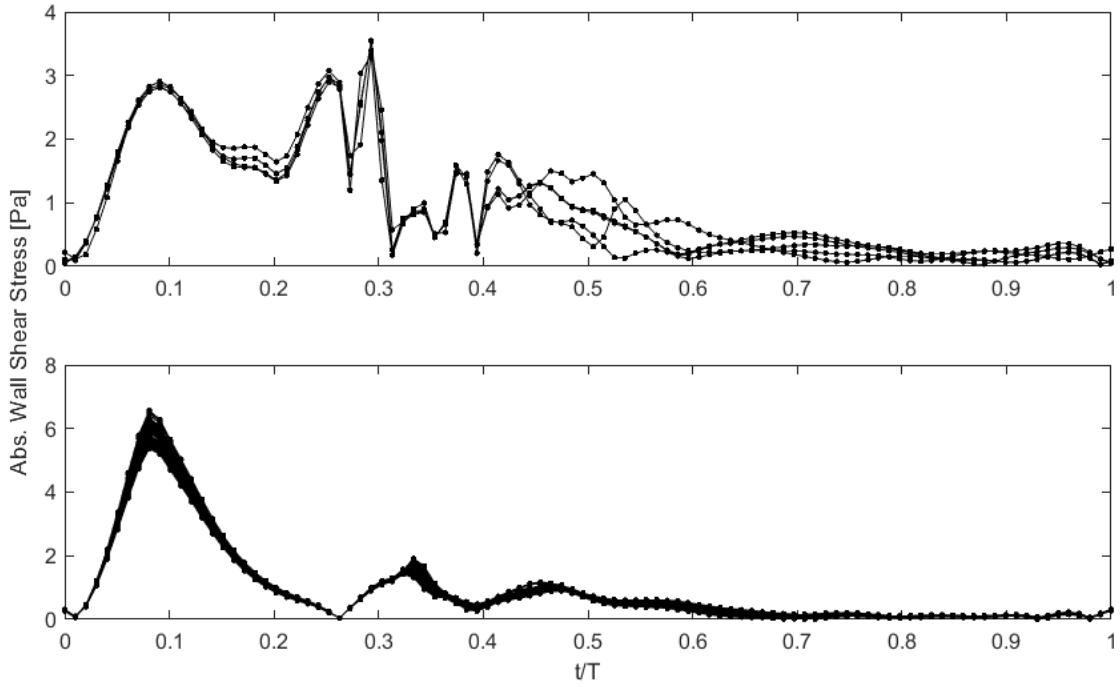

Figure 6 Primary results. t is time and T is the heart cycle duration. Top (Bottom) shows 10 (100) examples of simulation results at measurement point C (J) (see fig. 1). Each set of connected dots (data points) corresponds to one simulation with one parameter set (see also Appendix D).

usually not encountered in rheological experiments, and their corresponding Riemann prior might not necessarily be well defined or convenient.

In the case of the Carreau-model, the Riemann prior turned out to be improper, i.e. non-normalizable. However, a weakly informative likelihood ensured a proper posterior. Note that a flat prior, or a prior of the form $\propto 1/\lambda$ (both are improper), here would have yielded an improper (non-normalizeable) posterior as the likelihood alone was not informative enough. This would thus refuse meaningful parameter estimates and viscosity estimates (due to divergent integrals) without a strong prior. In other words, the authors were not aware of other a priori knowledge, that would justify to cut off heavy tails of the likelihood. This also means, that the results, both for viscosity and also the wall shear stresses, would depend strongly on the choice for the hyperparameters (boundaries) of such a strong prior. The importance of the prior thus strongly depends on the information in the data. In our case, particularly information on the value of the zero-shear limit viscosity, η_0, and the slope, λ, was not unambiguous. The matter could also be addressed by more precise measurements at lower shear rates, but would be limited by the yield stress [51]. In fact, our model does not consider (visco-)elastic properties below the yield stress at all. The existence of the plateau in the extrapolation in fig. 5b to lower shear rates is thus questionable, as it is only a result of the underlying assumptions of the Carreau model but not backed by experimental data. It is further unknown how in vitro conditions in the rheometer differ from in vivo conditions.

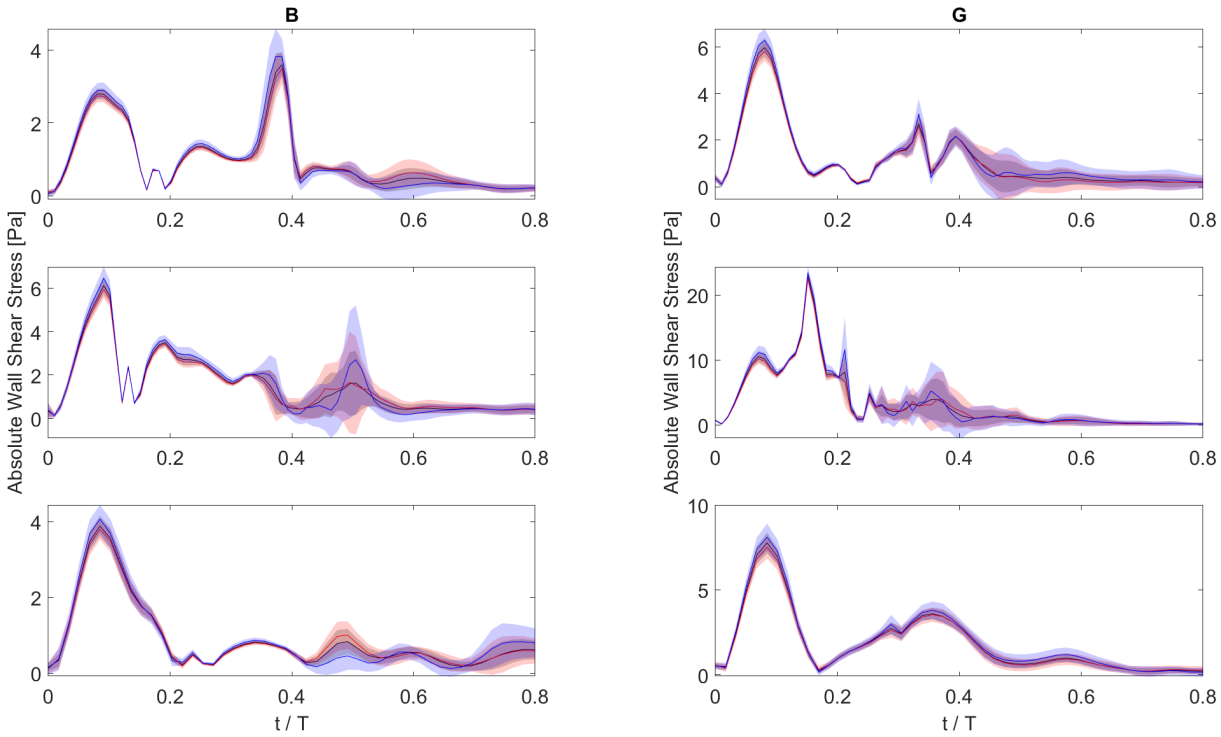

Figure 7 Measurement Point B (left) and G (right) with non-linear viscosity from fig. 4a. t is time and T is the heart cycle duration. Top: Low Reynolds & Low Womersley number. Middle: High Reynolds & Low Womersley number. Bottom: High Reynolds & High Womersley number. Black is the population average, and red/blue is specific for volunteer 1/3. The shaded areas are the corresponding uncertainty bands (1 standard deviation).

A further problem exists in the definition of blood. While the macroscopic view tempts to accept blood as a liquid, the microscopic view identifies blood as a suspension. Suspension properties affect flow properties in small conduits[52], e.g. through red blood cell arrangement[53], and may be effective also when a blood portion flows through e.g. a dissected aortic wall. Flow skewness, unsteadiness or possibly turbulence disturb the homogeneity of blood further[54,55,56], which makes blood a very dynamic material.

The simulations here are idealized and do not capture turbulence, fluid-structure interactions, or arterial branches or other complex features of physiological geometries. Shear-thinning effects are possibly more important in more complex simulations.

The comparison of the wall shear stresses of different persons (fig. 7) depends, here, on the assumption that the probability density function for the viscosity parameters for different persons is located in roughly the same region of parameter space. This allows to use one surrogate model for all. For person-specific viscosity data that is far outside the uncertainty bands in fig. 4a, this assumption would not hold, and one would need to construct person-specific surrogate models. This would also affect the estimate for the Reynolds-equivalent Newtonian viscosity, and subsequently the wall shear stress. The assumption was reasonable for the available data, however inter-personal variability of viscosity might in truth be much larger than what was found

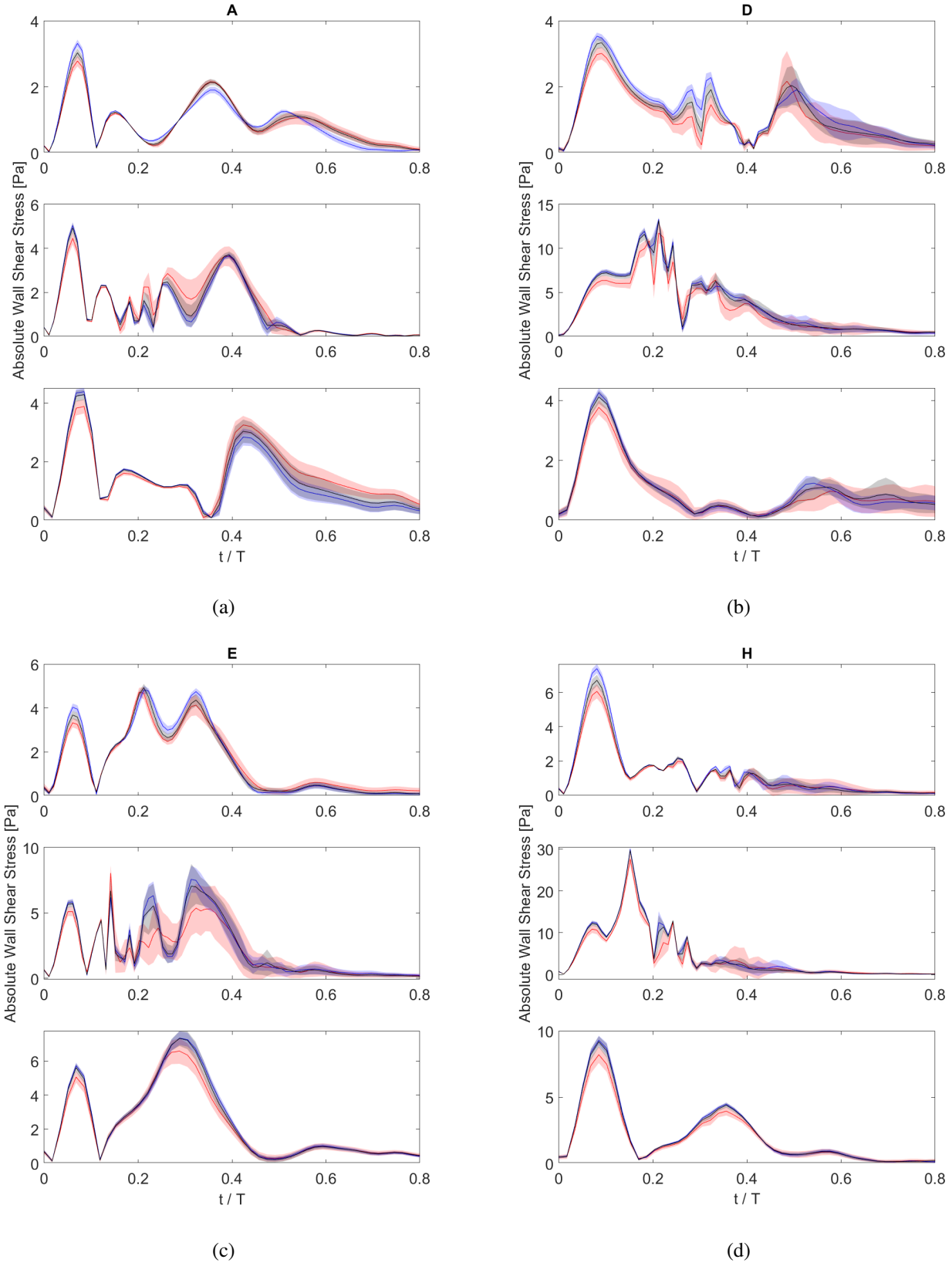

Figure 8 Measurement Point A/D/E/H (subfigures (a,b,c,d)). t is time and T is the heart cycle duration. In each, the top panel shows the result for Low Reynolds & Low Womersley number. Middle panel: High Reynolds & Low Womersley number. Bottom panel: High Reynolds & High Womersley number. Red: Carreau model. Blue: Reynolds-equivalent Newtonian model. Black: Simple Newtonian. The shaded areas are the corresponding uncertainty bands (1 standard deviation). Population-averaged statistics have been used.

here. That would require either personalized surrogate models, or the construction of surrogate models in larger regions of the parameter space. We used roughly 3 times the amount of simulation data for surrogate construction than typically recommended for Polynomial Chaos Expansions, however the surrogate's uncertainty could in principle be reduced with even more data. Standard paradigms in Uncertainty Quantification usually do require some measure of 'trustworthiness' for the surrogate, but usually neglect this uncertainty in the quantity of interest entirely. Unaffected by that, wall shear stress uncertainty here is mostly rooted in rheological uncertainty.

Lastly, a clear, general recommendation for a Newtonian or a non-Newtonian model is difficult also from this perspective. We have shown that the uncertainties in the wall shear stress can be significantly underestimated by Newtonian model and have quantified the associated trade-off for a given amount of simulation data of wall shear stresses. However, the required accuracy of this uncertainty quantification strongly depends on the specific use case, the quantity of interest, etc. The interplay of rheological uncertainties with other sources of uncertainties, e.g. boundary conditions or geometry reconstructions, have not been considered in this study.

5 | CONCLUSIONS

We have derived a consistent and rigorous method to estimate (non-)linear rheological parameters of blood and associated uncertainties in aortic hemodynamics based on Bayesian Probability Theory. We achieve robust estimates despite the large interpersonal variability via consistent inclusion of prior knowledge such as rescaling invariance. The uncertainty quantification of the non-Newtonian model was made practically feasible via a surrogate model and surrogate uncertainties were incorporated. We consider three different comparisons: (i) Newtonian vs. non-Newtonian rheology, (ii) person-specific vs. population averages and (iii) moderate activity vs. at rest, reflected by different parameters characterizing the inlet conditions.

Our quantities of interest were the wall shear stresses since these are believed to be linked to pathologies such as aortic dissection. However, the statistical theory can be applied without modification to e.g. pressure or flow field. Several representative measurement points were selected over a simplified aortic geometry.

The uncertainties of the non-Newtonian model were then compared to the uncertainties of two Newtonian models, a simple Newtonian model and a Reynolds number-equivalent Newtonian model. The estimation for the Reynolds-equivalent Newtonian model has been subjected to yield a flow regime comparable to the corresponding non-Newtonian flow, i.e. equal Reynolds numbers and Womersley numbers at the aortic root. This assumption ensured a fair and sound comparison on the same footing. We note that a rejection of this assumption would either result in unreasonably high uncertainties for the Newtonian viscosity, demand an arbitrary pre-selection of data points or parameters, or require to use entirely different data in the first place (as was done for the simple Newtonian model, Sec. 2.2.3).

The results show that uncertainties can be considerably underestimated by the Newtonian models as compared to the non-Newtonian model. However, also the opposite can occur, i.e. the Newtonian models overestimate the uncertainty. This seems counter-intuitive since the non-Newtonian model has four uncertain parameters while the Newtonian models only have one uncertain parameter. Note that we do not claim that one model is less uncertain than another in general. We merely quantify the error associated to certain model assumptions in the uncertainty quantification of the simulation. This is not necessarily the error of the simulation itself.

The effect is attributed to the larger uncertainties of the non-Newtonian viscosity at low shear rates, as compared to uncertainties at high shear rates or at the representative shear rate defining the Newtonian models. The larger uncertainties at low shear rates are attributed either to higher inter-personal variability or less informative data in that regime. This too implies that the Newtonian models underestimate the uncertainty. The issue may be settled by more precise determination of viscosity parameters by e.g. repeated or more precise measurements, particularly at low shear rates.

Our first conclusion is, that a non-Newtonian model should be considered because the Newtonian models can significantly underestimate the uncertainties. However this is not the general rule, as in some cases it can be the other way around. Our second conclusion is that either using population-averaged parameters for the viscosity is sufficient, or more precise or repeated person-specific measurements of blood viscosity are necessary if meaningful person-specific simulations are desired.

What remains open is the interaction of the rheological uncertainties with inlet conditions' uncertainties, geometric uncertainties and the dynamic motion of the aortic wall. These uncertainties are not necessarily additive, as was found by[26] for a Newtonian viscosity, and can be understood on the same grounds as why a viscosity model with four uncertain parameters is not necessarily more uncertain than a viscosity model with one uncertain parameter. We hypothesize that the found discrepancy in the uncertainties might be more pronounced in more complex, realistic geometries since low shear rates will become more frequent. This further suggests to pay more attention to the elastic behaviour below the yield stress.

ACKNOWLEDGEMENT

This work was funded by Graz University of Technology (TUG) through the LEAD Project "Mechanics, Modeling, and Simulation of Aortic Dissection" (biomechaorta.tugraz.at), supported by GCCE: Graz Center of Computational Engineering and HPC resources of TUG ZID.

CONFLICT OF INTEREST

The authors declare to have no conflicts of interest.

ETHICS

We followed a protocol approved by the local ethics committee, "Ethikkommission der Medizinischen Universität Wien," under ethical clearance number 2114/2019. The volunteers provided informed and written consent.

DATA ACCESSIBILITY

The data and codes are accessible[48] at Zenodo Digital Repository via: https://doi.org/10.5281/zenodo.4733649

AUTHOR CONTRIBUTIONS

SR and TSM conceived and designed the study. UW designed and performed the shear-rheometric experiments. TSM designed and performed the CFD simulations with support by GB. SR designed, derived the theory and implemented the computer code for the statistical analysis with support by WvdL. SR, TM, GB and WvdL participated in data analysis. SR and TSM wrote the manuscript with editing by GB, WvdL and UW. All authors contributed to the discussions.

References

1. Benjamin EJ, et al. . Heart Disease and Stroke Statistics—2019 Update: A Report From the American Heart Association. *Circulation* 2019; 139(10). doi: 10.1161/cir.0000000000000659

2. Erbel R, Alfonso F, Boileau C, et al. Diagnosis and management of aortic dissection: Task Force on Aortic Dissection, European Society of Cardiology. *European Heart Journal* 2001; 22(18): 1642–1681. doi: 10.1053/euhj.2001.2782

3. Robicsekand F, Thubrikar MJ. Hemodynamic considerations regarding the mechanism and prevention of aortic dissection. *The Annals of Thoracic Surgery* 1994; 58(4): 1247–1253. doi: 10.1016/0003-4975(94)90523-1

4. Malek AM, Alper S, S. Izumo M. Hemodynamic Shear Stress and Its Role in Atherosclerosis. *JAMA* 1999; 282(21): 2035. doi: 10.1001/jama.282.21.2035

5. Wan Ab Naim WN, Ganesan PB, Sun Z, Chee KH, Hashim SA, Lim E. A perspective review on numerical simulations of hemodynamics in aortic dissection. *The Scientific World Journal* 2014; 2014. doi: 10.1155/2014/652520

6. Cho Y, Kensey KR. Effects of the non-Newtonian viscosity of blood on flows in a diseased arterial vessel. Part 1: Steady flows. *Biorheology* 1991; 28(3-4): 241–262. doi: 10.3233/BIR-1991-283-415

7. Merrill EW. Rheology of blood. *Physiological Reviews* 1969; 49(4): 863–888. doi: 10.1152/physrev.1969.49.4.863

8. Perktold K, Resch M, Florian H. Pulsatile Non-Newtonian Flow Characteristics in a Three-Dimensional Human Carotid Bifurcation Model. *Journal of Biomechanical Engineering* 1991; 113(4): 464–475. doi: 10.1115/1.2895428

9. Pedley TJ. *The Fluid Mechanics of Large Blood Vessels*. Cambridge University Press . 1980

10. Ku DN. Blood flow in arteries. *Annual Review of Fluid Mechanics* 1997; 29(1): 399–434. doi: 10.1146/annurev.fluid.29.1.399

11. Rodkiewicz CM, Sinha P, Kennedy JS. On the Application of a Constitutive Equation for Whole Human Blood. *Journal of Biomechanical Engineering* 1990; 112(2): 198–206. doi: 10.1115/1.2891172

12. Tu C, Deville M. Pulsatile flow of non-Newtonian fluids through arterial stenoses. *Journal of Biomechanics* 1996; 29(7): 899–908. doi: 10.1016/0021-9290(95)00151-4

13. Gijsen F, Allanic E, Vosse v. dF, Janssen J. The influence of the non-Newtonian properties of blood on the flow in large arteries: unsteady flow in a 90 degree curved tube. *Journal of Biomechanics* 1999; 32(7): 705–713. doi: 10.1016/s0021-9290(99)00014-7

14. Razavi A, Shirani E, Sadeghi M. Numerical simulation of blood pulsatile flow in a stenosed carotid artery using different rheological models. *Journal of Biomechanics* 2011; 44(11): 2021–2030. doi: 10.1016/j.jbiomech.2011.04.023

15. Najm HN. Uncertainty quantification and polynomial chaos techniques in computational fluid dynamics. *Annual Review of Fluid Mechanics* 2009; 41: 35–52. doi: 10.1146/annurev.fluid.010908.165248

16. Eck V, Donders W, Sturdy J, et al. A guide to uncertainty quantification and sensitivity analysis for cardiovascular applications. *International Journal for Numerical Methods in Biomedical Engineering* 2016; 32(8): e02755. e02755 cnm.2755doi: 10.1002/cnm.2755

17. Ghanem RG, Owhadi H, Higdon D. *Handbook of uncertainty quantification*. Springer . 2017

18. O'Hagan A. Bayesian analysis of computer code outputs: A tutorial. *Reliability Engineering and System Safety* 2006; 91(10-11): 1290–1300. doi: 10.1016/j.ress.2005.11.025

19. von der Linden W, Dose V, von Toussaint U. *Bayesian Probability Theory: Applications in the Physical Sciences*. Cambridge University Press. 1 ed. 2014.

20. Jaynes ET. *Probability Theory: The Logic of Science*. Cambridge University Press . 2003

21. Boccadifuoco A, Mariotti A, Celi S, Martini N, Salvetti MV. Uncertainty quantification in numerical simulations of the flow in thoracicaortic aneurysms. In: NTU Athens. Proceedings of the VII European Congress on Computational Methods in Applied Sciences and Engineering (ECCOMAS Congress 2016); 2016. doi: 10.7712/100016.2254.10164

22. Bozzi S, Morbiducci U, G. D, et al. Uncertainty propagation of phase contrast-MRI derived inlet boundary conditions in computational hemodynamics models of thoracic aorta. *Computer Methods in Biomechanics and Biomedical Engineering* 2017; 20(10): 1104–1112. doi: 10.1080/10255842.2017.1334770

23. Antiga L, Ene-Iordache B, Remuzzi A. Computational geometry for patient-specific reconstruction and meshing of blood vessels from MR and CT angiography. *IEEE Transactions on Medical Imaging* 2003; 22(5): 674–684. doi: 10.1109/tmi.2003.812261

24. Maher G, Fleeter C, Schiavazzi D, Marsden A. Geometric Uncertainty in Patient-Specific Cardiovascular Modeling with Convolutional Dropout Networks. arXiv: 2009.07395; 2020.

25. Pereira J, Moura eJS, Ervilha A, Pereira J. On the uncertainty quantification of blood flow viscosity models. *Chemical Engineering Science* 2013; 101: 253–265. doi: 10.1016/j.ces.2013.05.033

26. Sankaran S, Kim HJ, Choi G, Taylor CA. Uncertainty quantification in coronary blood flow simulations: Impact of geometry, boundary conditions and blood viscosity. *Journal of Biomechanics* 2016; 49(12): 2540–2547. doi: 10.1016/j.jbiomech.2016.01.002

27. Xiu D, Karniadakis G. The Wiener-Askey polynomial chaos for stochastic differential equations. *SIAM J. Sci. Comput.* 2005; 27(3): 1118–1139.

28. O'Hagan A. Polynomial chaos: a tutorial and critique from a statistician's perspective. Available: http://tonyohagan.co.uk/academic/pdf/Polynomial-chaos.pdf, accessed 25.06.2019; 2013.

29. O'Hagan A. Curve Fitting and Optimal Design for Prediction. *Journal of the Royal Statistical Society. Series B (Methodological)* 1978; 40(1): 1–42. doi: 10.2307/2984861

30. Rasmussen C, Williams. C. *Gaussian Processes for Machine Learning*. The MIT Press . 2006

31. Bird RB, Armstrong RC, Hassager O. *Dynamics of Polymeric Liquids - Volume 1 Fluid Mechanics*. A Wiley-Interscience puplication . 1987.

32. Ostwald W. Ueber die rechnerische Darstellung des Strukturgebietes der Viskositaet. *Kolloid-Zeitschrift* 1929; 47: 176–187. doi: 10.1007/BF01496959

33. Casson N. A flow equation for the pigment oil suspensions of the printing ink type. *Rhelogy of Disperse Systems* 1959; 5: 84–102.

34. Carreau PJ. Rheological Equations from Molecular Network Theories. *Transactions of the Society of Rheology* 1972; 16(1): 99-127. doi: 10.1122/1.549276

35. Böhme G. *Strömungsmechanik nicht-newtonscher Fluide (Mechanics of non-Newtonian Fluids, in German)*. B.G. Teubner-Verlag . 2000.

36. Peacock J, Jones T, Tock C, Lutz R. The onset of turbulence in physiological pulsatile flow in a straight tube. *Experiments in Fluids* 1998; 24(1): 1–9. doi: 10.1007/s003480050144

37. Metzner AB, Reed JC. Flow of non-newtonian fluids—correlation of the laminar, transition, and turbulent-flow regions. *American Institute of Chemical Engineers* 1955; 1(4): 434–440. doi: 10.1002/aic.690010409

38. Womersley JR. Method for the calculation of velocity, rate of flow and viscous drag in arteries when the pressure gradient is known. *Journal of Physiology* 1955; 127: 553–563. doi: 10.1113/jphysiol.1955.sp005276

39. Gosling RG, King DH. Arterial Assessment by Doppler-shift Ultrasound. *Proceedings of the Royal Society of Medicine* 1987; 6(67): 447–449.

40. Kesmarky G, Kenyeres P, Rabai M, Toth K. Plasma viscosity: A forgotten variable. *Clinical Hemorheology and Microcirculation* 2008; 39: 243–246. doi: 10.3233/CH-2008-1088

41. Alastruey J, Xiao N, Fok H, Schaeffter T, Figueroa CA. On the impact of modelling assumptions in multi-scale, subject-specific models of aortic haemodynamics. *Journal of the Royal Society Interface* 2016; 13(119). doi: 10.1098/rsif.2016.0073

42. Goldsmith H. Poiseuille Medal Award Lecture: From papermaking fibers to human blood cells. *Biorheology* 1993; 30(3–4): 165–190. doi: 10.3233/BIR-1993-303-404

43. Stalder AF, Frydrychowicz A, Russe MF, et al. Assessment of flow instabilities in the healthy aorta using flow-sensitive MRI. *Journal of magnetic resonance imaging* 2011; 33: 839–846. doi: 10.1002/jmri.22512

44. Stein PD, Sabbah HN. Turbulent blood flow in the ascending aorta of humans with normal and diseased aortic valves.. *Circulation Research* 1976; 39(1): 58–65. doi: 10.1161/01.res.39.1.58

45. Sivia D, Skilling J. *Data Analysis: a Bayesian Tutorial*. OUP Oxford . 2006.

46. O'Hagan A, Kennedy MC, Oakley JE. Uncertainty analysis and other inference tools for complex computer codes. *Bayesian Staistics 6* 1999: 503–524.

47. Ranftl S, von der Linden W. Bayesian Surrogate Analysis and Uncertainty Propagation with Explicit Surrogate Uncertainties and Implicit Spatio-temporal Correlations. arXiv: 2101.04038; 2021.

48. Ranftl S, Müller TS, Windberger U, von der Linden W, Brenn G. Data and codes for 'A Bayesian Approach to Blood Rheological Uncertainties in Aortic Hemodynamics'. Zenodo Digital Repository; 2021. Accessible via https://doi.org/10.5281/zenodo.4733649

49. Panteleev MA, Korin N, Reesink KD, et al. Wall shear rates in human and mouse arteries: Standardization of hemodynamics for in vitro blood flow assays: Communication from the ISTH SSC subcommittee on biorheology. *Journal of Thrombosis and Haemostasis* 2021; 19(2): 588-595. doi: https://doi.org/10.1111/jth.15174

50. Oshinski JN, Ku DN, Mukundan Jr S, Loth F, Pettigrew RI. Determination of wall shear stress in the aorta with the use of MR phase velocity mapping. *Journal of Magnetic Resonance Imaging* 1995; 5(6): 640-647. doi: https://doi.org/10.1002/jmri.1880050605

51. Picart C, Piau JM, Galliard H, Carpentier P. Human blood shear yield stress and its hematocrit dependence. *Journal of Rheology* 1998; 42(1): 1-12. doi: 10.1122/1.550883

52. Thurston GB. The viscosity and viscoelasticity of blood in small diameter tubes. *Microvascular Research* 1976; 11(2): 133-146. doi: https://doi.org/10.1016/0026-2862(76)90045-5

53. Kumar A, Henríquez Rivera RG, Graham MD. Flow-induced segregation in confined multicomponent suspensions: effects of particle size and rigidity. *Journal of Fluid Mechanics* 2014; 738: 423–462. doi: 10.1017/jfm.2013.592

54. Reneman R, Arts T, Hoeks A. Wall Shear Stress – an Important Determinant of Endothelial Cell Function and Structure – in the Arterial System in vivo. *Journal of Vascular Research* 2006; 43. doi: 10.1159/000091648

55. Mchedlishvili G, Maeda N. Blood Flow Structure Related to Red Cell Flow: Determinant of Blood Fluidity in Narrow Microvessels. *The Japanese Journal of Physiology* 2001; 51(1): 19-30. doi: 10.2170/jjphysiol.51.19

56. Saqr KM, Tupin S, Rashad S, et al. Physiologic blood flow is turbulent. *Scientific Reports* 2020; 10(1): 1–12. doi: 10.1038/s41598-020-72309-8

How to cite this article: Ranftl, S., Müller, T.S., Windberger, U., Brenn, G. and von der Linden, W. (2021), A Bayesian Approach to Blood Rheological Uncertainties in Aortic Hemodynamics, *IJNMBE*, *2021;00:pp*. Special Issue 'Modeling the biomechanics of the normal and diseased aorta'

APPENDIX

A A BRIEF INTRODUCTION TO BAYESIAN PROBABILITY THEORY

Probability is a measure of the truthfulness of a proposition, a statement which can either be true or false. BPT is thus a generalization of Boolean algebra to partial truths. It is a consistent and rigorous framework to treat uncertainties of any kind, be it due to noisy experimental data, missing information, unknown parameters or uncertain models.

Like in Boolean algebra, propositions can be combined by logical AND, which will here be denoted by a comma ",". Let b and d be two such propositions, where b could e.g. be the proposition specifying a parameter and d the proposition specifying the values of a data set. We distinguish the probability $p(b)$ that b is true without further information, and the conditional probability $p\big(b \mid d\big)$ that b is true given further information denoted by d, e.g. measurement data. Strictly speaking there are no un-conditional probabilities. They always depend on the so-called background information that specifies the problem, the meaning of the parameters and all additional information. For example, $\mathcal{I}$ will among others contain the information that we use the Carreau model for the shear rate dependent non-linear viscosity. It could also contain the information that the WSS z is computed by FVM simulations. Along with the necessary Carreau parameters $\boldsymbol{a}$ the quantity $p\big(z \mid \boldsymbol{a}, \mathcal{I}\big)$ is the probability density (pdf) for obtaining the result z in a FVM simulation, based on the parameters $\boldsymbol{a}$. In this case the distribution is extremely narrow, as fluctuations are merely due to numerical errors. Another example would be that $\tilde{\mathcal{I}}$ encodes the information that we will use a surrogate model to compute the WSS corresponding to Carreau parameters $\boldsymbol{a}$. The corresponding pdf is $p\big(z \mid \boldsymbol{a}, \tilde{\mathcal{I}}\big)$. We see the background information is crucial. Nevertheless, we will omit it where it is easily possible, in order to keep the formulas transparent.

From the sum rule and the product rule [19], we find the marginalization rule for continuous variables

$$p\big(d\big) = \int p\big(d \mid b\big) p\big(b\big) db \,, \tag{A1}$$

and Bayes' theorem

$$p\big(b, d\big) = p\big(d \mid b\big) p\big(b\big) = p\big(b \mid d\big) p\big(d\big) \,, \tag{A2}$$

which allows to solve inverse problems consistently. The meaning of the four terms in Bayes' theorem are: $p\big(b\big)$ is the prior probability for a before taking the experiment data into account. $p(d \mid bx)$ is the so-called likelihood, which is the probability for measuring d given the underlying true model parameters b. The likelihood is usually known as it quantifies the uncertainties of the experiment. Strictly speaking, an experiment is meaningless, if the inaccuracies cannot be quantified. We are interested in the posterior, $p(a \mid d)$, i.e. the probability that b is the underlying model parameter in the light of the measured data d. The last term in eq. 39, the so-called data evidence $p(d)$, is independent of b, and not of concern for our considerations. The ν-th

moment of b is defined by

$$\langle b^{\nu} \rangle = \int b^{\nu} p\big(b\big) db \,. \tag{A3}$$

The first moment is the mean value of b and is commonly used as an estimate for the unknown parameter b. The uncertainty of this estimate is given by the standard deviation

$$\Delta b = \sqrt{\langle b^2 \rangle - \langle b \rangle^2} \tag{A4}$$

B RIEMANNIAN PRIOR

Given a likelihood $p\big(\boldsymbol{d} \mid \boldsymbol{a}\big)$ the Riemannian metric is given by

$$g_{ij} = \int p(\boldsymbol{d} \mid \boldsymbol{a}) \frac{\partial^2}{\partial a_i \partial a_j} \ln\left(p(\boldsymbol{d} \mid \boldsymbol{a})\right) \, dV_{\boldsymbol{d}} = \left\langle \frac{\partial^2}{\partial a_i \partial a_j} \ln\left(p(\boldsymbol{d} \mid \boldsymbol{a})\right) \right\rangle \tag{B5}$$

and the Riemannian prior is given by

$$p(\boldsymbol{a}) = \frac{1}{Z} \Big| \det(g) \Big|^{1/2} \,. \tag{B6}$$

It is the most uninformative and yet symmetry-preserving prior, in the sense that it is invariant under re-parameterisation. We want to determine the Riemannian metric based on the marginal likelihood in eq. 25.

$$p\big(\boldsymbol{\eta} \mid \dot{\boldsymbol{\gamma}}, \boldsymbol{a}, \alpha\big) = \frac{1}{Z'} (\chi^2)^{-\frac{N}{2}} \,, \tag{B7}$$

and

$$\ln(p(\boldsymbol{d} \mid \boldsymbol{a})) = -\frac{N}{2} \ln(\chi^2) + \text{const.} \tag{B8}$$

To simplify the notation, for the index pair (m, n), which are the shear rate and volunteer indices, we introduce a compound index l. Then the misfit has the standard form

$$\chi^2 = \sum_{l=1}^{N} \frac{(\eta_l - f(\gamma_l | \boldsymbol{a}))^2}{\hat{\sigma}_l^2} \,. \tag{B9}$$

The partial derivatives are

$$\frac{\partial^2}{\partial a_i \partial a_j} \ln(p(\boldsymbol{d} \mid \boldsymbol{a})) = \frac{N}{\chi^2} \sum_l \frac{1}{\hat{\sigma}_l^2} \left[(d_l - f(\dot{\gamma}_l \mid \boldsymbol{a})) \frac{\partial^2 f(\dot{\gamma}_l \mid \boldsymbol{a})}{\partial a_i \partial a_j} - \frac{\partial f(\dot{\gamma}_l \mid \boldsymbol{a})}{\partial a_i} \frac{\partial f(\dot{\gamma}_l \mid \boldsymbol{a})}{\partial a_j} \right] \tag{B10}$$

$$- \frac{N}{(\chi^2)^2} \left[\sum_l \frac{(d_l - f(\dot{\gamma}_l \mid \boldsymbol{a}))}{\hat{\sigma}_l^2} \frac{\partial f(\dot{\gamma}_l \mid \boldsymbol{a})}{\partial a_i} \right] \left[\sum_l \frac{(d_l - f(\dot{\gamma}_l \mid \boldsymbol{a}))}{\hat{\sigma}_l^2} \frac{\partial f(\dot{\gamma}_l \mid \boldsymbol{a})}{\partial a_j} \right] \tag{B11}$$

Here

$$\left\langle \frac{d_l - f(\dot{\gamma}_l \mid \boldsymbol{a})}{\chi^2} \right\rangle = 0 \,. \tag{B12}$$

and $\left\langle h(\chi^2) \right\rangle$ for an arbitrary function h is independent of the parameters $\boldsymbol{a}$. Both results are obtained by the substitution $d_n - f(\dot{\gamma}_n \mid \boldsymbol{a}) \to t_n$ in the integrals. Therefore,

$$\left\langle \frac{\partial^2}{\partial a_i \partial a_j} \ln(p(\boldsymbol{d} \mid \boldsymbol{a})) \right\rangle = N \sum_l \frac{\partial f(\dot{\gamma}_l \mid \boldsymbol{a})}{\partial a_i} \frac{\partial f(\dot{\gamma}_l \mid \boldsymbol{a})}{\partial a_j} \left\langle \frac{1}{\chi^2} \right\rangle \tag{B13}$$

$$- N \sum_l \left\langle \frac{(d_l - f(\dot{\gamma}_l \mid \boldsymbol{a})^2}{(\chi^2)^2} \right\rangle \frac{\partial f(\dot{\gamma}_l \mid \boldsymbol{a})}{\partial a_i} \frac{\partial f(\dot{\gamma}_l \mid \boldsymbol{a})}{\partial a_j} \tag{B14}$$

Again, based on the previous substitution, the average in the second line is independent of the parameters. Hence,

$$\left\langle \frac{\partial^2}{\partial a_i \partial a_j} \ln(p(\boldsymbol{d} \mid \boldsymbol{a})) \right\rangle = c \sum_l \frac{1}{\hat{\sigma}_l^2} \frac{\partial f(\dot{\gamma}_l \mid \boldsymbol{a})}{\partial a_i} \frac{\partial f(\dot{\gamma}_l \mid \boldsymbol{a})}{\partial a_j} \,. \tag{B15}$$

Now we insert the original indices, resulting in

$$g_{ij} = c N_p \sum_{m=1}^{N_m} \frac{1}{\hat{\sigma}_m^2} \frac{\partial f(\dot{\gamma}_m \mid \boldsymbol{a})}{\partial a_i} \frac{\partial f(\dot{\gamma}_m \mid \boldsymbol{a})}{\partial a_j} \,. \tag{B16}$$

The remaining derivatives can easily be determined by routine mathematics.

C DISTRIBUTION OF REYNOLDS AND WOMERSLEY NUMBERS

The resulting distribution of Reynolds numbers and Womersley numbers as an intermediate result prior fig. 4b are shown in fig. C1a,C1b, both skewed and asymmetric with a heavier tail towards higher numbers. Particularly the Reynolds numbers vary over a large range, however the physiological states moderate activity / at rest (low Reynolds number / high Reynolds number) clearly reside in their respective regimes.

D DESIGN OF COMPUTER EXPERIMENT

From a regular grid of 50x50x50x50, the 40000 most probable population-averaged parameter combinations were pre-selected with the aim to 'zoom in' on the posterior, or in other words; to avoid simulating parameter combinations that carry a negligible probability weight. However this may introduce a bias, and 40000 simulations would take roughly 80 cpu-years. To tackle both issues, this pre-selection was then thinned out by randomly selecting 100 out of those 40000, mitigating the bias, covering a larger volume and the outer regions of the posterior while avoiding utterly implausible parameter combinations and retaining computational feasibility. An illustration of this sample set is shown Fig. D2b and D2a. Remark: The spreading / mean distance / discrepancy of the pre-selection samples can be controlled with the grid size and the number (here 40000) of samples included

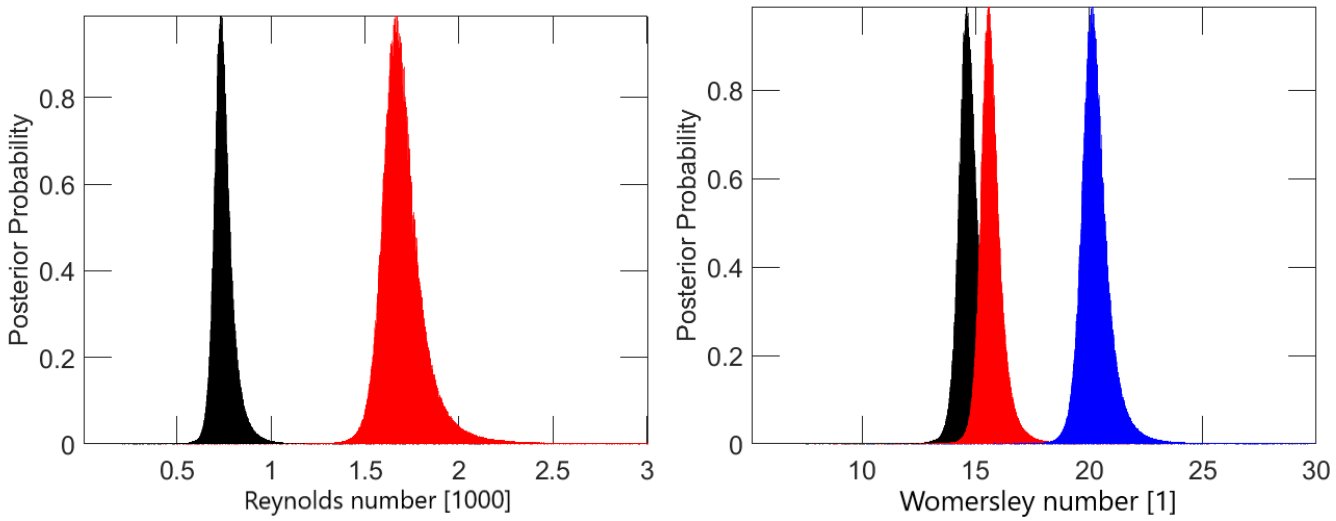

(a) (b)

Figure C1 (a) Population-averaged posterior probability distribution for the generalized Reynolds number according to Tab. 1 and Eq. 37. Black (Red): Physiological State 1 (2 & 3). (b) Population-averaged posterior probability distribution for the Womersley number according to Tab. 1 and Eq. 37. Black/Red/Blue: Physiological State 1/2/3

in the 'lottery' . The number of samples drawn from the lottery usually is given by the computational budget. This procedure is heuristic but educated, and in contrast to classic latin hyper cube sampling allows to consider the posterior and improve the surrogate where it is important. An alternative procedure would be to draw samples directly from the posterior via Markov Chain Monte Carlo, where one sample is taken each after a specific Markov time has passed.

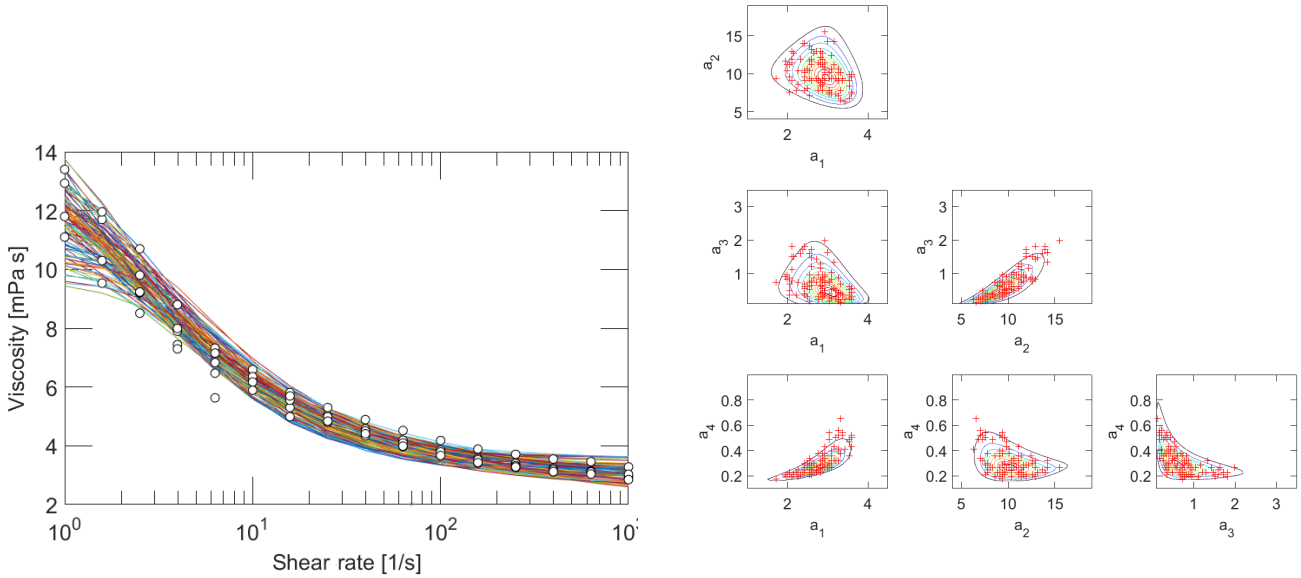

(a) (b)

Figure D2 (a) Family of viscosity models for the computer experiments. Each line corresponds to one cross (=parameter sample) in Fig. D2b. The circles are measurement data from the shear-rheometric experiments. (b) Position of the samples for the computer experiments in parameter space relative to the population-averaged joint posterior. The semi-randomized selection procedure is described in the text. The samples roughly span roughly over the posterior volume.

E TIME-AVERAGED SUMMARIES

Let $\boldsymbol{\tau} = (\tau_x, \tau_y, \tau_z)^T$ be the wall shear stress vector. Then the time-average of the absolute value of the wall shear stress (TAWSS), $||\boldsymbol{\tau}||$, is defined as

$$\tilde{\tau}_w = \frac{1}{T} \int_{t=0}^{T} ||\boldsymbol{\tau}|| dt$$

Note that $||\boldsymbol{\tau}|| = w$ as used in Sec. 3. The mean is

$$\langle \tilde{\tau}_w \rangle = \int \tilde{\tau}_w(\boldsymbol{a})\ p\big(\boldsymbol{a} \mid \boldsymbol{d}_{\text{exp}}\big) dV_{\boldsymbol{a}}\ .$$

Here, $p\big(\boldsymbol{a} \mid \boldsymbol{d}_{\text{exp}}\big)$ is the population-averaged posterior of fig. 3b. The oscillatory shear index (OSI) is defined as

$$I_S = \frac{1}{2}\left(1 - \frac{||\int_{t=0}^{T} \boldsymbol{\tau} dt||}{\int_{t=0}^{T} ||\boldsymbol{\tau}|| dt}\right)$$

The mean then is

$$\langle I_S \rangle = \int I_S(\boldsymbol{a})\ p\big(\boldsymbol{a} \mid \boldsymbol{d}_{\text{exp}}\big) dV_{\boldsymbol{a}}\ .$$

The Relative Residence Time then is

$$T_R \propto \frac{1}{I_S}$$

and the proportionality constant here shall be set to 1. The mean of T_R is quantified analogously to the mean of I_S. The uncertainty of these estimates is given by equations analogous to eq. 40 and eq. 41. Distinct surrogate models are necessary either for the vector components or each index directly. Here, it turned out that building separate surrogate models for each index directly was most efficient. Results are shown below in table E1-E3. For $\tilde{\tau}_w$, the Newtonian models mostly overestimate the value of the index, but underestimate its uncertainty as compared to the Carreau model in all 3 cases. For I_S, the Newtonian models mostly underestimate the uncertainty, but no such observation was made for the index value. T_R behaves analogously to I_S.

Table E1 Time-averaged absolute wall shear stress ($\langle\tilde{\tau}_w\rangle$) [$mPa$] including uncertainties.Location indicates the probe spot (see fig. 1), Carreau, Reynolds-equivalent (RE)-Newton and Simple Newton refers to the three compared rheological models introduced in sections 2.2.1, 2.2.2 and 2.2.3. The number 1/2/3 refers to the physiological cases (inlet conditions) documented in table 2.

	Case 1			Case 2			Case 3		
	Carreau	RE-Newton	Simple Newton	Carreau	RE-Newton	Simple Newton	Carreau	RE-Newton	Simple Newton
Location					$\langle\tilde{\tau}_w\rangle \pm \Delta\tilde{\tau}_w$				
A	71 ± 6	69 ± 2	72 ± 2	99 ± 10	91 ± 3	93 ± 5	194 ± 19	158 ± 17	171 ± 26
B	76 ± 2	92 ± 4	81 ± 5	117 ± 9	140 ± 9	136 ± 11	100 ± 5	105 ± 5	102 ± 4
C	95 ± 7	101 ± 5	95 ± 3	290 ± 20	325 ± 10	319 ± 13	148 ± 16	173 ± 14	170 ± 16
D	81 ± 12	99 ± 6	91 ± 6	252 ± 18	280 ± 10	278 ± 12	113 ± 14	120 ± 8	120 ± 9
E	120 ± 7	122 ± 3	117 ± 5	148 ± 20	172 ± 9	167 ± 12	225 ± 13	245 ± 9	239 ± 10
F	91 ± 4	108 ± 3	98 ± 5	174 ± 11	197 ± 6	193 ± 10	178 ± 7	188 ± 3	187 ± 5
G	88 ± 10	110 ± 8	96 ± 9	254 ± 21	284 ± 13	277 ± 13	194 ± 14	214 ± 8	207 ± 9
H	91 ± 7	103 ± 5	96 ± 5	310 ± 33	351 ± 19	338 ± 19	198 ± 13	215 ± 8	210 ± 9
I	131 ± 4	140 ± 3	134 ± 2	186 ± 6	198 ± 9	193 ± 7	240 ± 11	262 ± 7	257 ± 8
J	91 ± 4	108 ± 3	98 ± 5	174 ± 11	197 ± 6	193 ± 10	178 ± 7	188 ± 3	187 ± 5

Table E2 Oscillatory shear index ($\langle I_S \rangle$) [1] including uncertainties. Location indicates the probe spot (see fig. 1), Carreau, Reynolds-equivalent (RE)-Newton and Simple Newton refers to the three compared rheological models introduced in sections 2.2.1, 2.2.2 and 2.2.3. The number 1/2/3 refers to the physiological cases (inlet conditions) documented in table 2.

	Case 1			Case 2			Case 3		
	Carreau	RE-Newton	Simple Newton	Carreau	RE-Newton	Simple Newton	Carreau	RE-Newton	Simple Newton
Location					$\langle I_S \rangle \pm \Delta I_S$				
A	0.222 ± 0.010	0.276 ± 0.017	0.237 ± 0.015	0.282 ± 0.020	0.320 ± 0.019	0.307 ± 0.024	0.132 ± 0.019	0.182 ± 0.025	0.166 ± 0.034
B	0.035 ± 0.008	0.050 ± 0.004	0.042 ± 0.005	0.061 ± 0.028	0.044 ± 0.010	0.047 ± 0.013	0.036 ± 0.028	0.066 ± 0.034	0.059 ± 0.028
C	0.148 ± 0.037	0.087 ± 0.022	0.126 ± 0.022	0.007 ± 0.007	0.012 ± 0.007	0.011 ± 0.005	0.422 ± 0.073	0.428 ± 0.031	0.427 ± 0.039
D	0.036 ± 0.029	0.025 ± 0.012	0.033 ± 0.016	0.011 ± 0.009	0.012 ± 0.005	0.010 ± 0.005	0.115 ± 0.047	0.100 ± 0.023	0.124 ± 0.034
E	0.166 ± 0.025	0.198 ± 0.024	0.186 ± 0.020	0.283 ± 0.058	0.274 ± 0.036	0.275 ± 0.036	0.131 ± 0.010	0.136 ± 0.006	0.135 ± 0.006
F	0.321 ± 0.020	0.300 ± 0.006	0.297 ± 0.013	0.120 ± 0.059	0.120 ± 0.016	0.127 ± 0.017	0.418 ± 0.010	0.450 ± 0.011	0.441 ± 0.014
G	0.360 ± 0.045	0.388 ± 0.030	0.359 ± 0.028	0.207 ± 0.082	0.200 ± 0.033	0.198 ± 0.031	0.345 ± 0.032	0.348 ± 0.016	0.351 ± 0.012
H	0.223 ± 0.062	0.226 ± 0.029	0.216 ± 0.033	0.145 ± 0.066	0.119 ± 0.021	0.122 ± 0.024	0.367 ± 0.035	0.373 ± 0.010	0.381 ± 0.013
I	0.460 ± 0.015	0.442 ± 0.005	0.443 ± 0.010	0.465 ± 0.040	0.445 ± 0.026	0.455 ± 0.024	0.303 ± 0.018	0.325 ± 0.010	0.322 ± 0.013
J	0.321 ± 0.020	0.300 ± 0.006	0.297 ± 0.013	0.120 ± 0.059	0.120 ± 0.016	0.127 ± 0.017	0.418 ± 0.010	0.450 ± 0.011	0.441 ± 0.014

Table E3 Relative residence time ($\langle T_R \rangle$) [1] including uncertainties. Location indicates the probe spot (see fig. 1), Carreau, Reynolds-equivalent (RE)-Newton and Simple Newton refers to the three compared rheological models introduced in sections 2.2.1, 2.2.2 and 2.2.3. The number 1/2/3 refers to the physiological cases (inlet conditions) documented in table 2.

	Case 1			Case 2			Case 3		
	Carreau	RE-Newton	Simple Newton	Carreau	RE-Newton	Simple Newton	Carreau	RE-Newton	Simple Newton
Location					$\langle T_R \rangle \pm \Delta T_R$				
A	4.5 ± 0.2	3.6 ± 0.2	4.2 ± 0.2	3.5 ± 0.3	3.1 ± 0.2	3.3 ± 0.3	7.6 ± 1.1	5.6 ± 0.8	6.3 ± 1.3
B	29.0 ± 6.1	20.2 ± 1.8	24.3 ± 2.7	17.2 ± 6.9	23.5 ± 4.5	22.7 ± 5.0	28.5 ± 14.7	19.0 ± 8.3	20.4 ± 7.7
C	6.9 ± 1.8	12.6 ± 4.3	8.2 ± 1.5	156.8 ± 93.3	113.2 ± 63.2	114.2 ± 49.2	2.4 ± 0.5	2.4 ± 0.2	2.4 ± 0.2
D	35.2 ± 26.3	47.3 ± 17.8	35.7 ± 13.6	111.1 ± 95.4	103.8 ± 49.7	145.9 ± 95.5	9.7 ± 3.7	10.5 ± 2.2	8.8 ± 2.6
E	6.1 ± 0.9	5.1 ± 0.5	5.4 ± 0.6	3.6 ± 0.8	3.7 ± 0.5	3.7 ± 0.4	7.7 ± 0.6	7.4 ± 0.3	7.4 ± 0.3
F	3.1 ± 0.2	3.3 ± 0.1	3.4 ± 0.1	8.5 ± 3.7	8.5 ± 1.1	8.0 ± 1.1	2.4 ± 0.1	2.2 ± 0.1	2.3 ± 0.1
G	2.8 ± 0.3	2.6 ± 0.2	2.8 ± 0.2	5.0 ± 2.4	5.1 ± 0.8	5.2 ± 0.8	2.9 ± 0.3	2.9 ± 0.1	2.9 ± 0.1
H	4.6 ± 1.2	4.5 ± 0.5	4.7 ± 0.7	7.0 ± 3.9	8.6 ± 1.4	8.4 ± 1.5	2.7 ± 0.2	2.7 ± 0.1	2.6 ± 0.1
I	2.2 ± 0.1	2.3 ± 0.0	2.3 ± 0.1	2.2 ± 0.2	2.3 ± 0.1	2.2 ± 0.1	3.3 ± 0.2	3.1 ± 0.1	3.1 ± 0.1
J	3.1 ± 0.2	3.3 ± 0.1	3.4 ± 0.1	8.5 ± 3.7	8.5 ± 1.1	8.0 ± 1.1	2.4 ± 0.1	2.2 ± 0.1	2.3 ± 0.1